UNCLASSIFIED

SECURITY CLASSIFICATION OF THIS PAGE *(When Data Entered)*

REPORT DOCUMENTATION PAGE		READ INSTRUCTIONS BEFORE COMPLETING FORM
1. REPORT NUMBER RPI Math. Rep. No. 153	2. GOVT ACCESSION NO.	3. RECIPIENT'S CATALOG NUMBER
4. TITLE *(and Subtitle)* Sensitivity of a Passive Tracking Algorithm to Input Variations		5. TYPE OF REPORT & PERIOD COVERED 6. PERFORMING ORG. REPORT NUMBER
7. AUTHOR(s) W. L. Siegmann, M. J. Jacobson, and P. Bilizarian		8. CONTRACT OR GRANT NUMBER(s) N00014-76-C-0288
9. PERFORMING ORGANIZATION NAME AND ADDRESS Rensselaer Polytechnic Institute Troy, New York 12180-3590		10. PROGRAM ELEMENT, PROJECT, TASK AREA & WORK UNIT NUMBERS NR 386-606
11. CONTROLLING OFFICE NAME AND ADDRESS Office of Naval Research, Code 425 Department of the Navy Arlington, Virginia 22217		12. REPORT DATE 15 August 1985 13. NUMBER OF PAGES 49
14. MONITORING AGENCY NAME & ADDRESS*(if different from Controlling Office)*		15. SECURITY CLASS. *(of this report)* 15a. DECLASSIFICATION/DOWNGRADING SCHEDULE

16. DISTRIBUTION STATEMENT *(of this Report)*

This document has been approved for public release and sale; its distribution is unlimited.

17. DISTRIBUTION STATEMENT *(of the abstract entered in Block 20, if different from Report)*

18. SUPPLEMENTARY NOTES

19. KEY WORDS *(Continue on reverse side if necessary and identify by block number)*

Passive Tracking
Multipath Propagation
Tracker Sensitivity
Linear Arrays

20. ABSTRACT *(Continue on reverse side if necessary and identify by block number)*

The sensitivity of a passive horizontal-tracking algorithm to variations in input measurements is investigated. The algorithm determines estimates for depth, range, bearing, horizontal speed, course, and frequency for a cw acoustic source moving with constant velocity at fixed depth. The receiver is a horizontal linear array towed at a constant depth. Both source and receiver move in the upper portion of a deep ocean and are separated by a relatively short range. Dominant acoustic signals are presumed to arrive

DD FORM 1 JAN 73 1473 EDITION OF 1 NOV 65 IS OBSOLETE
S/N 0102-LF-014-6601

UNCLASSIFIED

SECURITY CLASSIFICATION OF THIS PAGE *(When Data Entered)*

along two upper-ocean ray paths. The algorithm uses a new combination of input quantities, including multipath information, Doppler frequency shifts, and array directional measurements. Procedures are developed for analyzing effects of input-measurement errors on source localization. The robustness of the algorithm to small variations in acoustic measurements and environmental parameters is demonstrated for a variety of source-receiver configurations. Variance estimates of position and motion are obtained in terms of input-measurement variances. Bounds on tracker performance are developed for measurements that are affected by noise. Results from the several types of analyses corroborate the sensitivity characteristics of the algorithm.

Sensitivity of a Passive Tracking Algorithm to Input Variations

by

W. L. Siegmann, M. J. Jacobson,
and P. Bilazarian

RPI math. Rep. No. 153

Department of Mathematical Sciences

Rensselaer Polytechnic Institute

Troy, New York 12180-3590

RPI Math. Rep. No. 153

15 August 1985

This work was sponsored by

Code 425, Office of Naval Research

Contract No. N00014-76-C-0288

NR 386-606

ABSTRACT

The sensitivity of a passive horizontal-tracking algorithm to variations in input measurements is investigated. The algorithm determines estimates for depth, range, bearing, horizontal speed, course, and frequency for a cw acoustic source moving with constant velocity at fixed depth. The receiver is a horizontal linear array towed at a constant depth. Both source and receiver move in the upper portion of a deep ocean and are separated by a relatively short range. Dominant acoustic signals are presumed to arrive along two upper-ocean ray paths. The algorithm uses a new combination of input quantities, including multipath information, Doppler frequency shifts, and array directional measurements. Procedures are developed for analyzing effects of input-measurement errors on source localization. The robustness of the algorithm to small variations in acoustic measurements and environmental parameters is demonstrated for a variety of source-receiver configurations. Variance estimates of position and motion are obtained in terms of input-measurement variances. Bounds on tracker performance are developed for measurements that are affected by noise. Results from the several types of analyses corroborate the sensitivity characteristics of the algorithm.

INTRODUCTION

Many procedures have been developed to determine passively the motion of an underwater acoustic source. They involve a variety of acoustic quantities measured at one or more receivers, which typically consist of arrays of sensors. In familiar bearings-only tracking, direct measurements are made, at several observation times, of received signal-arrival angles. These are subsequently processed to obtain estimates of source position and velocity.[1-3] A quantity which has received considerable attention recently is the time delay (or travel-time difference) between ray arrivals at sensor pairs.[4-8] For example, Ref. 8 describes how time delays observed at a linear array may be converted into source-distance and direction information. Another measured quantity (or descriptor) is the received frequency, which is employed in Doppler tracking.[9] Some tracking methods have exploited a combination of descriptors, such as multipath time delays in conjunction with bearing measurements.[10]

In a previous investigation,[11] effects of a moving cw source on acoustic total field received at short ranges, was studied. The receiver was fixed on the surface, and the total field consisted of two bottom-bounce rays emanating from the constant-velocity source moving above the SOFAR axis. A key feature was the occurence of brief, regularly spaced changes in total-field phase rate, referred to as phase roll. We present here a passive tracking algorithm using as one of its descriptors the quasi-period of phase rolls. The algorithm determines estimates for depth, range, bearing, horizontal speed, course, and frequency for a cw source moving with constant velocity at fixed depth. The receiver is a horizontal linear array which is towed at fixed depth. Both source and receiver move in the upper portion of a deep ocean and are separated by relatively short ranges. The horizontal-tracking algorithm

involves a new combination of input information from direct and surface-reflected ray paths. Specifically, the descriptors include the multipath phase-roll quasi-period as well as the signal-arrival angle and received frequency from the direct-ray arrival. In order to show the essential features of our procedure in as simple a context as possible, the sound speed is taken as uniform in the ocean region from the surface to the deeper of the source and receiver, and the ocean surface is assumed horizontal.

Many factors can contribute to measurement errors in underwater source localization and tracking. One is the omnipresence of noise, which corrupts all measurements to some degree, and arises from a variety of environmental and systems causes. Other factors involve the receiving array of sensors, which is subject to physical influences which limit its performance in estimating descriptors such as signal-arrival angle. Examples are the individual independent motions of array sensors[12] or sub-arrays,[13] array element failure and errors in amplitude and phase between hydrophone channels,[14] and bending of the linear array.[15] Furthermore, aspects of systems software and signal processing also contribute to descriptor errors. For example, measurement and processing times must be small enough so that source or receiver motion does not appreciably affect descriptor values. A discussion of this characteristic in relation to received frequency measurements appears in Ref. 9. Finally, the neglect of variations in various environmental features involved in tracking procedures can lead to errors. Examples of environmental influences which have been investigated are sound-speed or bottom-slope variations,[16,17] and turbulence in the propagation medium.[18] Often, the aforementioned descriptor errors are either inherently random or must be treated as random. However, some error influences can be treated in a deterministic manner. As just one example, Ref. 19 contains an analysis of non-random eddy-induced variations on

source bearing-angle determination by a horizontal linear array. It is necessary as well to analyze the effects on tracking procedures of these types of errors, which are not necessarily random but, in fact, may arise from modeling simplifications.

The principal purpose of this paper is investigation of the sensitivity of the aforementioned horizontal-tracking algorithm to variations in inputs, including both acoustic descriptors and other algorithm parameters. The analysis of effects of input measurement errors on output predictions for source-localization quantities can typically be divided into two stages. The first is determination of input variations resulting from the specific error source, and the second is the study of input variations on various outputs using the algorithm equations. For examples, error analyses of time-delay measurements corrupted by noise are combined with second stages, relating various output errors to time-delay errors, in Refs. 5 and 7. For tracking procedures in which the relations between the outputs and measured inputs are well understood (e.g., the "planar" problem in Ref. 7), emphasis is on the first stage. However, for a new tracking algorithm as considered here, some basic issues associated mainly with the second stage are essential to investigate. One of these is algorithm robustness, i.e., its ability to yield reasonably accurate output information for small imprecision in its inputs. Another related matter is the determination of which outputs are more sensitive to small or relatively large input perturbations. Consequently, in one portion of our sensitivity investigation, we address these issues by studying propagation of non-random input-measurement errors, resulting from unspecified influences, on algorithm outputs. We describe rather general procedures for this error-propagation analysis, and use them in a variety of tracking scenarios. In another portion, we determine relations between various

quantities associated with random input and output errors. We consider also the particular influence of noise on input measurements, to determine bounds on tracker performance in terms of signal-to-noise ratio.

In Sec. I, we develop a nonlinear system of equations for the horizontal-tracking algorithm, relating the aforementioned descriptors to parameters which describe source position, motion, and frequency. Section II addresses the sensitivity of solutions to the algorithm equations to input-measurement errors. An essential feature of the methods discussed is a development of linear approximations expressing algorithm output errors in terms of various input variations. In Sec. III, the robustness of the algorithm is demonstrated for the propagation of input errors in various source-receiver scenarios. Some of these scenarios consist of special cases, in which source and receiver configurations are restricted in some manner. The effect of random input variations for these special scenarios is discussed in Sec. IV. The influence of varying degrees of descriptor-variation correlation on correlation between output errors is studied. We also develop Cramer-Rao lower bounds for the variances of estimates of certain outputs associated with input errors influenced by Gaussian white noise. Finally, major results are summarized in Sec. V.

I. HORIZONTAL-TRACKING ALGORITHM

We present here a horizontal-tracking algorithm for the passive determination of position, motion, and frequency of a cw point source S, based on measurements taken at a linear receiving array R. The source (or receiver) is submerged at constant depth D_s (or D_r), and moves in a straight line with constant speed v_s (or v_r). The tracking algorithm could be adapted to more general source and receiver motions, with non-linear paths and non-constant

speeds, by piecewise-linear approximation. Source and receiver depths are less than about 400 m, and the horizontal distance between S and R is less than about 10 km. The source is assumed to emit an omnidirectional signal which possesses a dominant single frequency f_s (in Hz). The sound speed c in the ocean region between the surface and $\max(D_s,D_r)$ is taken to be constant, and conditions for the validity of ray theory are assumed. Thus, the source signal travels in linear ray paths. For the S-R geometries considered here, we regard the received acoustic field to be dominated by the direct and surface-reflected rays, denoted by "one" and "two", respectively.

When both rays arrive at R at some time t_n (in s), the direct ray is emitted from S at time $t_{1,n}$, while the surface-reflected ray emanates at a slightly different time, $t_{2,n}$. Figure 1(a) shows a projection into a vertical plane at time t_1. Vertical projections of the one and two rays are shown here, along with projected directions of S and R (solid arrows). Figure 1(b) illustrates a projection into a horizontal plane at times t_1 and t_2. The horizontal separation (range) between S and R at time t_n is denoted by R_n. Angle β_{rn} (or β_{sn}) is measured from the horizontal projection of the path of R (or S) to the "line of sight" between S and R at t_n. Both β_{rn} and β_{sn} are measured positive clockwise, and are taken in the interval $-\pi < \beta_{rn}, \beta_{sn} \leq \pi$ [for example, in Fig. 1(b), $\beta_{rn} > 0$ and $\beta_{sn} < 0$].

Source location, motion, and frequency are determined at time t_n by values of the six parameters D_s, R_n, β_{rn}, β_{sn}, v_s, and f_s. We note that parameters R, β_r, and β_s vary with time, while D_s, v_s, and f_s have been taken to be time-invariant. In order to find these parameter values, we use certain descriptors measured at R at, or close to, two distinct times t_n, $n = 1,2$. These descriptors include both directional information from the linear array and particular acoustic information, consisting of the period of multipath

phase variations and the Doppler-shifted received frequency for ray one. This formulation of the tracking algorithm, as well as the sensitivity analysis in subsequent sections, is extendable to the case of more than two measurement times. Utilization of more measurements would be expected to yield improved source localization and tracking estimates. However, we do not carry out this extension here.

We now develop equations at time t_n which relate our selected descriptors to the six source parameters mentioned above. We shall present later in this section relations which enable various parameters at time t_2 to be expressed in terms of those at time t_1. The directional information obtained from the linear horizontal receiving array is the signal-arrival angle ψ_n for the peak array output, which corresponds to the direct ray. Thus, the descriptor ψ_n is measured from the horizontal receiver trajectory [the solid arrow in Fig. 1(c)] to the direct ray arrival, with $0 \leq \psi_n \leq \pi$, and $\psi_n = \pi/2$ being broadside. The other line in Fig. 1(c) represents the horizontal projection of the direct ray at time t_n. It is close to, but not exactly the same as, the line of sight in Fig. 1(b), because of the S and R motion between times $t_{1,n}$ and t_n. The angle θ_n in Fig. 1(c) is the vertical angle at time t_n at R of the direct ray, and is measured positive clockwise from this line to the direct ray (note that θ_n may assume positive or negative values, $-\pi/2 < \theta_n < \pi/2$, depending on the relative depths of S and R). In Fig. 1(c), the angle β'_{rn} at time t_n is measured in a horizontal plane from the receiver path to the horizontal projection of the direct ray. It can be shown that β'_{rn} equals the previously defined angle β_{rn} plus a small correction. By approximating β'_{rn} by β_{rn}, it follows that

$$\cos \psi_n \doteq \cos \theta_n \cos \beta_{rn} \ . \tag{1}$$

The quantity cos θ_n in Eq. (1) can be expressed in terms of the unknowns D_s and R_n, so that

$$\cos \psi_n = \{1 + [(D_r - D_s)/R_n]^2\}^{-1/2} \cos \beta_{rn} , \tag{2}$$

which is the desired relation at time t_n between the descriptor ψ_n and three unknowns.

We turn next to the phase-roll period, an acoustic descriptor involving multipath information. It has been shown[11] for certain moving-source/fixed-receiver configurations that overall linear multipath phase, associated with two dominant bottom-reflected rays, is interrupted by rapid, regularly-spaced changes in phase rate. These nearly-periodic changes were shown to occur over time intervals that are from several to tens of seconds long. If S emits a signal proportional to $\sin(2\pi f_s t)$, where t is time in s, the received signal at R along the direct (m = 1) and surface-reflected (m = 2) paths can be expressed as

$$w_m(t) = A_m \sin 2\pi[f_s t - \phi_m(t)], \; m = 1,2 . \tag{3a}$$

The relative amplitudes A_m can be taken to be constant for time intervals of interest. Although w_m is not a sinusoidal function of time, Eq. (3a) expresses each arrival in the form of one with fixed frequency f_s and time-dependent phase $\phi_m(t)$ (in cycles):

$$\phi_m(t) = f_s \tau_m(t) - (m-1)/2, \; m = 1,2 . \tag{3b}$$

In Eq. (3b), $\tau_m(t)$ is the travel time of the signal along the mth ray, and the second term accounts for a surface phase shift of the m = 2 ray. The total acoustic field at R at time t is

$$W(t) = A(t) \sin 2\pi[f_s t - \Phi(t)] , \tag{4a}$$

where the multipath relative amplitude A(t) is

$$A(t) = A_1\{1 + k^2 + 2k \cos[\Delta\phi(t)]\}^{1/2} , \tag{4b}$$

and the total-field phase $\Phi(t)$ is

$$\Phi(t) = \phi_1(t) - \tan^{-1}(k \sin[\Delta\phi(t)]\{1 + k \cos[\Delta\phi(t)]\}^{-1}) . \tag{4c}$$

In Eqs. (4b) and (4c), $\tan^{-1}$ is the principal value of the inverse-tangent function, and

$$k = A_2/A_1, \ \Delta\phi(t) = \phi_1(t) - \phi_2(t) . \tag{4d}$$

By differentiating Eq. (4c) with respect to t and assuming $(t - t_n)$ to be sufficiently small so that $\phi_1(t)$, $\phi_2(t)$, and $\Delta\phi(t)$ may be expanded to linear terms in $(t - t_n)$, we obtain, for the multipath phase rate $\Phi'(t)$,

$$\Phi'(t) = f_s \tau'_{1,n} - f_s(\tau'_{1,n} - \tau'_{2,n})G , \tag{5a}$$

where

$$G \equiv k(k + \cos \Delta\phi)(1 + k^2 + 2k \cos \Delta\phi)^{-1} , \tag{5b}$$

and $\tau'_{m,n} = (d/dt)\tau_m(t)\big|_{t=t_n}$. From Eqs. (5a) and (5b), $\Phi'(t)$ repeats when $\Delta\phi$ changes by one cycle. Therefore, the phase-roll period P_n in s/cycle of Φ' is

$$P_n \equiv (f_s|\tau'_{1,n} - \tau'_{2,n}|)^{-1} , \tag{6}$$

where Eq. (6) follows from the linear [in $(t-t_n)$] approximation to $\Delta\phi$. By using trigonometry and expansions of order M^2Rc^{-1} and smaller, where Mach number M is $\max(v_s, v_r)/c$, accurate approximations for $\tau'_{1,n}$ and $\tau'_{2,n}$ may be found. We employ these approximations in Eq. (6) to obtain an equation relating P_n at time t_n to the six S parameters described previously:

$$P_n = cf_s^{-1}\left|(b_{1,n} - b_{2,n})(v_s \cos \beta_{sn} + v_r \cos \beta_{rn})\right|^{-1} , \tag{7a}$$

where

$$b_{m,n} \equiv \left(1 + \left\{\left[D_r - (-1)^{m+1}D_s\right]/R_n\right\}^2\right)^{-1/2}, \; m = 1,2 . \tag{7b}$$

Equations (6) and (7) suggest a connection of the phase-roll period to a differential-Doppler effect,[4] but we shall not discuss the similarities and differences between these phenomena here.

The final descriptor of interest is the received frequency of the direct ray arrival at time t_n. It is obtained by examining the power spectrum at R resulting from the emitted line spectrum (at frequency f_s). The finite-time power spectrum H(f) of the multipath arrival W(t) is found as a function of frequency f in the usual manner, with a time average over an interval of length T, where T is up to several tens of seconds, about $t = t_n$. It can be shown that H(f) has two distinct peaks, corresponding to the m = 1 and 2 ray arrivals. Moreover, H assumes the larger of its two peaks at frequency $f = f_{rn}$ for m = 1, since its amplitude is larger than that for m = 2. The quantity f_{rn} is given by

$$f_{rn} = f_s\left(1 - \dot{\tau}'_{1,n}\right) , \tag{8}$$

and $f_s\tau'_{1,n}$ in Eq. (8) is a Doppler-type shift in frequency of the direct arrival resulting from relative source-receiver motion. Using the approximation for $\tau'_{1,n}$ discussed before Eq. (7a), we obtain

$$f_{rn} = f_s\left[1 + c^{-1}b_{1,n}\left(v_s \cos \beta_{sn} + v_r \cos \beta_{rn}\right)\right] , \tag{9}$$

where $b_{1,n}$ is defined by Eq. (7b).

We have developed the three Eqs. (2), (7a), and (9), which relate three descriptors ψ_n, P_n, and f_{rn} at time t_n to six unknowns D_s, R_n, β_{rn}, β_{sn}, v_s, and f_s. To supplement these three equations at one time t_1, we propose that they be employed at an additional measurement time t_2. For this purpose, we make the reasonable assumption that S and R motion is linear over time intervals between one and several minutes. As discussed previously, measurements of the descriptor values have been assumed to require shorter intervals, of up to tens of seconds.

The linearity of the S and R tracks impose relations among geometric quantities R_n, β_{sn}, and β_{rn} at successive times. These relations produce a system of six equations in six unknowns (with n = 1). The solution to this system, combined with these relations, permits specification of S parameters at t_2 as well. We let $\Delta t_2 = t_2 - t_1$, Y_2 be the length of the line joining the horizontal projections of R at time t_1 and of S at time t_2 [see Fig. 1(b)], and η_2 be the angle shown in Fig. 1(b). It can be shown that the following equations, relating R_2, β_{s2}, and β_{r2} to various n = 1 unknowns, are valid:

$$R_2 = \left[Y_2^2 + (v_r \Delta t_2)^2 - 2Y_2 v_r \Delta t_2 (\cos \beta_{r1} \cos \eta_2 + \sin \beta_{r1} \sin \eta_2)\right]^{1/2}, \quad (10a)$$

where

$$Y_2 = \left[R_1^2 + (v_s \Delta t_2)^2 - 2R_1 v_s \Delta t_2 \cos \beta_{s1}\right]^{1/2}, \quad (10b)$$

$$\cos \eta_2 = \left[Y_2^2 + R_1^2 - (v_s \Delta t_2)^2\right]/2R_1 Y_2, \quad (10c)$$

and

$$\sin \eta_2 = (v_s \Delta t_2 \sin \beta_{s1})/Y_2 ; \quad (10d)$$

$$\cos \beta_{s2} = \left[R_1 \cos \beta_{s1} - v_s \Delta t_2 - v_r \Delta t_2 \cos(\beta_{r1} - \beta_{s1})\right]/R_2 ; \quad (11a)$$

and

$$\beta_{r2} = \beta_{s2} + \beta_{r1} - \beta_{s1} \, . \tag{12}$$

We omit tedious details of the derivation of Eqs. (10a)-(12) for various cases of β_{r1} and β_{s1}. These equations do remain valid if the subscript 2 is replaced by n, which enables extension of our tracking procedure to more than two measurement times.

In summary, the horizontal tracking algorithm involves the solution of the system of six nonlinear Eqs. (2), (7a), and (9) with n = 1,2, in terms of the six unknowns R_1, β_{s1}, β_{r1}, D_s, v_s, and f_s. Equations (10) through (12) are used to express R_2, β_{s2}, and β_{r2} in terms of these unknowns. The solution to this system for typical input values can be obtained numerically using, for example, a nonlinear least squares procedure.[20] We do not provide an investigation of existence and uniqueness of solutions to this system. This is because our principal interest here is in algorithm sensitivity, and also because implementation of such an algorithm could employ usefully measurements at additional times and equations for S/R paths consisting of multiple linear segments. Instead, we provide in Sec. III some typical examples of solutions to the system for various S/R scenarios. After solution at time t_1 is found, Eqs. (10)-(12) are again employed to determine source location parameters at the later time t_2.

II. ALGORITHM SENSITIVITY ANALYSIS

In this section, we present methods for analyzing the propagation of measurement errors in horizontal-tracking algorithm inputs on output values (i.e., source location, motion, and frequency parameters). The inputs consist of the descriptors ψ_n, P_n, and f_{rn}, n = 1,2, and the sound-speed parameter c. The Introduction described various influences on measurement

errors that can arise in tracking situations. The procedures here will be used to study output errors without specifying particular input-error causes. Input errors can either be deterministic or random in nature, such as those due to neglect of environmental features or noise, respectively. Our procedures are developed first for non-random types of measurement errors, so that they can be applied in Sec. III to study algorithm robustness and relative sensitivities of output errors to input variations. Later in this section, we present methods to be used in Sec. IV for random input variations.

We concentrate in this paper on examination of particular cases when only certain sets of input quantities are perturbed: specifically, (1) phase-roll periods and received frequencies, (2) signal-arrival angles, and (3) sound speed. The first set consists of quantities that are inherently related to travel-time variations due to source-receiver motion (so it is possible to interpret errors in them in terms of travel-time errors). The second set is comprised of measurements from the linear array, and errors in them could arise from various types of array biases. The third case is a source of ocean-environmental error in this model. We emphasize that our procedures are sufficiently general to apply to other combinations of perturbed inputs, including all the descriptors being perturbed simultaneously. However, focusing on the particular cases clarifies the sensitivity characteristics of the algorithm.

We denote by an overbar, and reference as "unperturbed", all input quantities with values obtained from a set of measurements, and, also, all corresponding output values determined from the tracking algorithm. All these unperturbed values play the role of an algorithm solution whose sensitivity to input perturbations is to be studied. Similarly, "perturbed" inputs and outputs are unbarred. Further, we use Δ to indicate input perturbations (for

example, $\Delta P_1 = P_1 - \bar{P}_1$ is a perturbation in phase-roll period at time t_1), as well as output errors (for example, $\Delta R_2 = R_2 - \bar{R}_2$ represents the error in range at time t_2). We also designate the output error vector $\underset{\sim}{h}_n$, n = 1,2, by

$$\underset{\sim}{h}_n \equiv \left(\Delta D_s,\ \Delta R_n,\ \Delta\beta_{rn},\ \Delta\beta_{sn},\ \Delta v_s,\ \Delta f_s\right) . \tag{13}$$

Finally, for source depth, range, and source speed, the relative output error is defined to be the output error divided by the unperturbed value, and is denoted by a χ followed by the appropriate parameter in parentheses [for example, $\chi(D_s) = \Delta D_s/\bar{D}_s$ is the relative error in source depth].

We now proceed to derive linear approximations for output errors in terms of input perturbations. These approximations are numerically efficient in that the nonlinear system of tracking equations only has to be solved once with unperturbed inputs. They are useful also for obtaining tractable analytical formulas in the subsequent study of both non-random and random input variations. Finally, although they are derived only for small input variations, numerical examples in Sec. III show them to be accurate for rather large input variations, as well. We first develop linear approximations for nondimensional output errors in terms of nondimensional input perturbations. These approximations are easily converted to dimensional ones, are themselves useful numerically, and are directly applicable later to comparisons of variances and covariances for random output errors and input variations. Nondimensional quantities using unperturbed input values are defined as follows:

$$p_n \equiv P_n/\bar{P}_1,\ f_n \equiv f_{rn}/\bar{f}_{r1},\ n = 1,2, \tag{14a}$$

and

$$C \equiv c/\bar{c},\ \bar{\varepsilon} \equiv \left(\bar{P}_1\bar{f}_{r1}\right)^{-1},\ \bar{v} \equiv \left(\bar{P}_1\bar{f}_{r1}\bar{v}_r\right)/\bar{c} . \tag{14b}$$

Dimensionless unknowns x_{jn}, for $1 \leq j \leq 6$ and $n = 1,2$, are defined to be

$$x_{1n} \equiv (\bar{D}_r - D_s)/R_n,\ x_{2n} \equiv (\bar{D}_r + D_s)/R_n,\ x_{3n} \equiv \beta_{rn},\ x_{4n} \equiv \beta_{sn},$$

$$x_{5n} \equiv (\bar{P}_1 \bar{f}_{r1} v_s)/\bar{c},\ x_{6n} \equiv f_s/\bar{f}_{r1} \ . \tag{14c}$$

Note that D_s and R_n can be recovered from x_{1n} and x_{2n} by

$$D_s = \bar{D}_r(x_{2n} - x_{1n})/(x_{1n} + x_{2n}),\ R_n = \bar{2}D_r/(x_{1n} + x_{2n}) \ . \tag{14d}$$

A nondimensional version of the tracking algorithm, Eqs. (2), (7a), and (9), is given for $n = 1,2$ by

$$(1 + x_{1n}^2)^{-1/2} \cos x_{3n} - \cos \psi_n = 0 \ , \tag{15a}$$

$$Cx_{6n}^{-1} \left| \left[(1+x_{1n}^2)^{-1/2} - (1+x_{2n}^2)^{-1/2} \right] (x_{5n} \cos x_{4n} + \bar{v} \cos x_{3n}) \right|^{-1}$$

$$- p_n = 0 \ , \tag{15b}$$

and

$$x_{6n}\left[1 + \bar{\varepsilon}\, C^{-1}(1+x_{1n}^2)^{-1/2}(x_{5n} \cos x_{4n} + \bar{v} \cos x_{3n})\right] - f_n = 0. \tag{15c}$$

Nondimensional output vectors $\underset{\sim}{x}_n$ are

$$\underset{\sim}{x}_n \equiv (x_{1n}, x_{2n}, x_{3n}, x_{4n}, x_{5n}, x_{6n}) \ , \ n = 1,2 \ , \tag{16}$$

and from Eqs. (10)-(12), formulas for the components of $\underset{\sim}{x}_2$ (not written here) can be obtained in terms of those of $\underset{\sim}{x}_1$. Finally, the nondimensional input-perturbation vector $\underset{\sim}{\delta}$, which can represent any of the three sets of perturbations described previously, is defined by

$$\underset{\sim}{\delta} \equiv (\delta_1, \delta_2, \delta_3, \delta_4, \delta_5, \delta_6) \ . \tag{17a}$$

For each set, component δ_i, i = 1,6, corresponds to the perturbation in the ith equation of Eqs. (15), written with the n = 1 equations preceding the n = 2 equations. For example, with nondimensional perturbations in phase-roll period Δp_n and received frequency Δf_n, n = 1,2, we have

$$\underset{\sim}{\delta} = (0,\Delta p_1,\Delta f_1,0,\Delta p_2,\Delta f_2) \ . \tag{17b}$$

Linear approximations for the nondimensional error vectors $\Delta\underset{\sim}{x}_n(n=1,2)$, applicable to all input-variation sets, are now written as follows. We express Eqs. (15) as

$$F_i(\underset{\sim}{x}_1,\underset{\sim}{\delta}) = 0, \ i = 1,6 \ , \tag{17c}$$

and let J be the 6 × 6 Jacobian matrix for Eqs. (17c). Then entry (i,j) of J is

$$J_{ij} = \partial F_i/\partial x_{j1} \ , \tag{17d}$$

where the partial derivatives are evaluated at $(\underset{\sim}{x}_1,\underset{\sim}{\delta}) = (\overline{\underset{\sim}{x}}_1,\underset{\sim}{0})$, and $\underset{\sim}{0}$ is the zero vector. We do not list the entries of J in this paper. We let E be the 6 × 6 matrix, the kth column of which consists of partial derivatives of the F_i with respect to δ_k evaluated at $(\underset{\sim}{x}_1,\underset{\sim}{\delta}) = (\overline{\underset{\sim}{x}}_1,0)$. For all three sets of input perturbations, the matrix E is diagonal. It can be shown by generalizing a scalar result[21] that a linear approximation to $\Delta\underset{\sim}{x}_1$, valid to order $\underset{\sim}{\delta}$, is

$$\Delta\underset{\sim}{x}_1 \doteq B_1\underset{\sim}{\delta} \ , \tag{18a}$$

where

$$B_1 \equiv -J^{-1}E \tag{18b}$$

and J^{-1} is the inverse of the Jacobian matrix. We note that Eqs. (18) may be solved numerically in an efficient manner by a factorization scheme[20] applied to

$$J(\Delta \underset{\sim}{x}_1) = - E\underset{\sim}{\delta} \ . \tag{19}$$

Numerical experience with Eq. (19) indicates that it generally produces more accurate solutions than a corresponding dimensional linear system derived from Eqs. (2), (7a), and (9). By using Eq. (18a), the expressions mentioned previously for $\underset{\sim}{x}_2$ in terms of $\underset{\sim}{x}_1$, and a linear expansion of $\Delta \underset{\sim}{x}_2$, we obtain similarly that

$$\Delta \underset{\sim}{x}_2 \doteq B_2 \, \underset{\sim}{\delta} \ , \tag{20a}$$

where

$$B_2 \equiv K \, B_1 \ . \tag{20b}$$

The 6 × 6 matrix K consists of partial derivatives of the components of $\Delta \underset{\sim}{x}_2$ evaluated at $\Delta \underset{\sim}{x}_1 = \underset{\sim}{0}$, and B_1 is given by Eq. (18b). From Eqs. (14c), (14d), (18a), and (20a), approximations for the dimensional error vectors $\underset{\sim}{h}_n$ of Eq. (13) are readily obtained:

$$\underset{\sim}{h}_n = \left[2\bar{D}_r (\bar{x}_{1n} + \bar{x}_{2n})^{-2} (\bar{x}_{1n} \Delta x_{2n} - \bar{x}_{2n} \Delta x_{1n}), \ - 2\bar{D}_r (\bar{x}_{1n} + \bar{x}_{2n})^{-2} \times \right.$$

$$\left. (\Delta x_{1n} + \Delta x_{2n}), \ \Delta x_{3n}, \ \Delta x_{4n}, (\bar{c}/\bar{P}_1 \bar{f}_{r1}) \Delta x_{5n}, \ \bar{f}_{r1} \Delta x_{6n} \right], \ n = 1,2 \ . \tag{21}$$

Approximations for various relative output errors χ follow immediately from Eq. (21).

We turn briefly to formulas useful in analyzing output errors that are associated with random input variations. All input perturbations and output errors are modeled as random variables, but without specification of their probability distributions. These random variables possess mean values of zero. Equations (18a) and (20a) imply that the nondimensional output-error random variables satisfy

$$\Delta \underset{\sim}{\dot{x}}_n = B_n \underset{\sim}{\delta} \ , \ n = 1,2 \ , \tag{22}$$

where the input error $\underset{\sim}{\delta}$ is a vector random variable, but the entries of B_n are non-random. Entry (i,j) of the 6 × 6 error covariance matrix[5] V associated with $\underset{\sim}{\delta}$ is

$$V_{ij} \equiv \left(\delta_i \delta_k\right) \ , \tag{23a}$$

where $\left(\ \right)$ is expectation. A similar equation holds for the error covariance matrix V_n associated with $\Delta \underset{\sim}{x}_n$. It can be shown[22] that V and V_n satisfy

$$V_n = B_n \, V \, \tilde{B}_n \ , \tag{23b}$$

where ~ denotes matrix transpose. Equation (23b) is the desired relationship, expressing output-error variances and covariances in terms of those of input perturbations.

III. ERROR PROPAGATION ANALYSIS

We analyze the sensitivity of the horizontal-tracking algorithm outputs to deterministic input-measurement errors in a variety of source-receiver configurations. Typical scenarios are displayed in top-views in Fig. 2. Scenario (A) shows S and R on headings which are perpendicular at time t_1, so that the range R between them shortens at a later time t_2. Scenario (B) is an example of diverging range, while S and R converge at varying rates in (C), (D), and (E). Unperturbed values for algorithm parameters, descriptors, and track outputs are given in Table I. In subsection A, we consider scenarios (A)-(C); in subsection B, we discuss scenarios (D) and (E), in which motion is confined to a vertical plane, along with a particular version of scenario (A). We remark that we considered numerous other cases as well, which are not reported here.

A. Example scenarios

For each of scenarios (A)-(C), track outputs were computed using the numerical procedure described in Sec. I for the full nonlinear system of algorithm Eqs. (2), (7a), and (9). The principal result of this subsection is that, for all scenarios, small perturbations of all algorithm inputs produce small variations in output estimates. For example, we display in Fig. 3(a) [or Fig. 3(b)] graphs of relative percentage errors in depth, range, and speed at time t_2 versus phase-roll period perturbation $\Delta P (\equiv \Delta P_1 = \Delta P_2)$, for scenario (A) [or (B)]. The value of frequency perturbation $\Delta f_r (\equiv \Delta f_{r1} = \Delta f_{r2})$ is 0.1 Hz, while ΔP varies from 0 to 3 s/cycle. These nearly-linear curves in Figs. 3(a) and 3(b) show that output errors are small, not only for small values of ΔP, but also for relatively large values. For example, Fig. 3(a) indicates that relative output errors are less than 8% for ΔP values corresponding to relative period errors up to about 20%. The speed error (or depth error) curve is the largest in Fig. 3(a) [or Fig. 3(b)], which shows that the relative magnitudes of output errors are dependent upon scenario. An example of an approximate error curve, computed using Eq. (21), is displayed in Fig. 3(b) as the upper long-dashed curve for range error. It shows the accuracy of the linear approximations to output errors, for both small and relatively large values of ΔP. Also, for scenarios (A)-(C), output errors were shown to be much less sensitive to changes in received frequencies than to phase-roll period perturbations.

All output predictions are relatively insensitive to small input variations. However, some outputs are more sensitive to larger variations in some inputs than in other inputs. For example, we show in Fig. 4 relative depth, range, and speed percentage errors at time t_2 in scenario (C). Figure 4(a) illustrates these output errors, with an ordinate scale up to 25%, versus

ΔP (with Δf_r = 0.1 Hz). Figure 4(b) shows the same errors, with ordinate up to 5%, versus $\Delta\psi$ ($\equiv \Delta\psi_1 = \Delta\psi_2$), where $\Delta\psi$ represents the measurement error of the signal-arrival angle. Results in Fig. 4 are typical for other scenarios, as well.

We turn now to the influence of various input perturbations on errors in bearing and course. In Fig. 5(a) [or Fig. 5(b)], graphs of bearing - and course - angle errors at time t_2 versus $\Delta\psi$ are displayed for scenario (B) [or scenario (C)]. Results show that bearing ($\Delta\beta_r$) and course ($\Delta\beta_s$) angle errors are comparable to signal-arrival angle perturbations. We found this conclusion to be widely applicable. It follows that the main influence of $\Delta\psi$ or $\Delta\beta_r$ occurs in algorithm Eq. (2). These errors in β_r influence, in turn, the errors in β_s in Eqs. (7a) and (9), where both these quantities are present. In Fig. 5(a) [or Fig. 5(b)] values of $\Delta\beta_{r2}$ are always greater (or less) than $\Delta\beta_{s2}$, which shows that relative error magnitude varies with scenario. In contrast to the comparable influence of $\Delta\psi$ on both $\Delta\beta_r$ and $\Delta\beta_s$, there is a significant difference in the effect of ΔP on these quantities. Small variations in phase-roll period yield small changes in $\Delta\beta_r$ and $\Delta\beta_s$, but larger values of ΔP produce significantly larger values in $\Delta\beta_s$ than in $\Delta\beta_r$ in all scenarios. For example, with scenario (C) at time t_2 and values of ΔP = 2 s/cycle (and Δf_r = 0.1 Hz), $|\Delta\beta_{s2}| = 3.0^\circ$, while $|\Delta\beta_{r2}| = 0.05^\circ$. Since $\Delta\psi$ is zero here, the relation between β_r and ψ in Eq. (2) evidently serves to diminish the influence of ΔP on $\Delta\beta_r$ in Eq. (7a).

The input perturbation which least affects output errors is Δc. For Δc values up to 10 ms^{-1} in scenarios (A)-(C), output errors are nearly zero.

B. Special tracking scenarios

We discuss here the sensitivity of output errors to input perturbations in particular types of tracking scenarios. Scenarios (D) and (E) in Fig. 2

have motion confined to a vertical plane, and we consider a variant of scenario (A) with perpendicular tracks at time t_1. These scenarios are "special" in that a priori knowledge is assumed for bearing angles β_{rn}, n = 1,2, course angles β_{sn}, n = 1,2, and source frequency f_s. For subsequent convenience, we also take receiver depth less than source depth. The motivation for investigating special tracking scenarios is to obtain tractable analytical expressions for output errors in terms of input perturbations. Furthermore, useful information may be obtained from these for both deterministic input variations in this subsection and for random variations in Sec. IV. Finally, certain insights into the robustness of the tracking algorithm in more general scenarios are gained by understanding sensitivity results in special tracking scenarios.

The a priori knowledge for special scenarios is useful to reduce the full tracking system, Eqs. (2), (7a), and (9), to three tractable nonlinear equations at time t_1. In this reduced system, descriptors ψ_1, P_1, and f_{r1} determine three source parameters D_s, R_1, and v_s via explicit formulas. The remaining unknown R_2 is then found from Eq. (10a). These formulas will not be presented here. Instead, the accurate linear approximations corresponding to Eq. (21) will be described. It can be shown that Eqs. (15) can be reduced to a nondimensional system of two equations in two unknowns x_{21} and x_{51}. By applying Eq. (21) to this system, approximations for output errors are obtained. For example, it can be shown that, for perturbations in period ΔP_1 and frequency Δf_{r1}, relative errors $\chi(D_s)$, $\chi(R_1)$, and $\chi(v_s)$ are

$$\chi(D_s) \doteq \left[(\bar{D}_s-\bar{D}_r)/\bar{D}_s\right]c_1(\gamma_1+\gamma_2) \ , \tag{24a}$$

$$\chi(R_1) \doteq - c_1(\gamma_1+\gamma_2) \tag{24b}$$

and

$$\chi(v_s) \doteq (\cos \bar{\beta}_{s1}/\cos \bar{\beta}_{r1})[\bar{c}(\bar{f}_{r1}-\bar{f}_s)/\bar{v}_s \bar{f}_s \cos \bar{\psi}_1]\gamma_2 , \tag{24c}$$

where the relative period and frequency variations are

$$\gamma_1 \equiv \Delta P_1/\bar{P}_1 \tag{24d}$$

and

$$\gamma_2 \equiv \Delta f_{r1}/(\bar{f}_{r1}-\bar{f}_s) . \tag{24e}$$

The quantity c_1 is

$$c_1 \equiv (\bar{R}_1/2\bar{D}_r)(\cos \bar{\beta}_{r1}/\cos \bar{\psi}_1)\{c_2/[1-(c_3 \cos \bar{\psi}_1)^2]^{1/2}\} , \tag{25a}$$

where

$$c_1 \equiv [1-(\bar{f}_s/\bar{f}_{r1})]/\{\bar{P}_1 \bar{f}_{r1}[1-(\bar{f}_s/\bar{f}_{r1}) - (1/\bar{P}_1 \bar{f}_{r1})]^2\} \tag{25b}$$

and

$$c_3 \equiv [1-(\bar{f}_s/\bar{f}_{r1}) - (1/\bar{P}_1\bar{f}_{r1})]/[1-(\bar{f}_s/\bar{f}_{r1})] . \tag{25c}$$

Values of $\bar{D}_s$, $\bar{R}_1$, and $\bar{v}_s$ in Eqs. (24)-(25) are found from the reduced system described at the start of this paragraph. We conclude from Eqs. (24a) and (24b) that under our assumption $\bar{D}_r < \bar{D}_s$, the magnitudes of relative errors in range are greater than those in source depth. Also, we note that relative error in source speed is influenced only by the received frequency perturbation, unlike relative errors in depth and range at time t_1.

For scenarios (A), (D), and (E), we found that typically small input perturbations resulted in small errors in all outputs. This result is entirely consistent with results in Sec. III A for more general *S-R* configurations. For example, we display in Fig. 6(a) [or Fig. 6(b)] graphs of percentage relative errors in source depth, speed, and range at times t_1 and t_2 versus $\Delta P \equiv \Delta P_1$ for special scenario (A) [or scenario (D)], with Δf_{r1} having the constant value 0.1 Hz. We show in Figs. 6 and 7 graphs obtained from Eqs.

(24)-(25) and from an approximation (not included explicitly here) for $\chi(R_2)$. Numerous numerical calculations indicate the good accuracy of these approximations. Figs. 6(a) and 6(b) demonstrate that output errors are small for both small and relatively large values of ΔP. A comparison of Figs. 3(a) and 6(a) indicates that these percentage errors are somewhat larger for the restricted scenario (A) than for the general case with scenario (A). We observe also various qualitative conclusions of the output error approximations in Figs. 6(a) and 6(b) as, for example, speed errors in both figures being independent of ΔP perturbations.

In the previous subsection, output errors were affected much more significantly by ΔP than by Δf_r perturbations. For the special scenarios here, frequency-measurement errors can influence output errors comparably to phase-roll period variations. This can be seen from Eqs. (24), since relative period and frequency errors, γ_1 and γ_2, assume values of comparable magnitude. Also, Fig. 7(a) [or Fig. 7(b)] shows the effect of Δf_r values up to 1 Hz (with ΔP = 1 sec) on percentage depth, range, and speed errors for restricted scenario (A) [or scenario (E)]. Similarly, the influence of the received angle perturbation on percentage errors in depth and range is considerably larger for the special scenarios than in subsection A.

Our analysis in this subsection has corroborated the conclusions in Sec. IIIA in that the tracking algorithm is generally robust for reasonable input perturbations. The investigation here was performed on a subsystem of the equations associated with the full algorithm. It also indicates that for larger input perturbations, certain output errors are typically much less with the full algorithm than with an algorithm based on the subsystem. Therefore, the full algorithm is better able to absorb larger input fluctuations and still produce good predictions. This suggests enhanced robustness of the full algorithm by incorporating measurements at more than two times.

IV. SENSITIVITY TO RANDOM VARIATIONS

We discuss relations between random input measurements and corresponding output errors for our tracking algorithm. Examples of possible sources of random influences on input-measurement errors are discussed in the Introduction. In subsection A, we study random output errors without specifying any particular input-error mechanism; in subsection B, we consider the specific effect of input noise variations. In order to present tractable formulas, we focus on special tracking scenarios as described in Sec. IIIB. However, we stress that the methods used with the special scenarios can be generalized to more general ones. We choose to analyze effects of phase-roll period and received frequency perturbations, at time t_1 and with zero means, on relative errors in source depth and speed. Random relative range errors are not included, since they can always be derived from relative source-depth errors.

A. Random error correlations

In Sec. II, it is noted that the period and received frequency are both related to travel-time variations due to S-R motion. It is reasonable, then, to expect that random influences which affect errors in one of these descriptors also produces errors in the other. We wish to describe the effect of varying correlation between perturbations in these descriptors on the correlation between output errors. Zero-mean random variables for nondimensional period and frequency variations are represented here by γ_1 and γ_2 in Eqs. (24d) and (24e), and by $\chi(D_s)$ and $\chi(v_s)$ for relative source depth and speed errors. The input-perturbation variances and covariance are $\sigma^2_{\gamma i} = E(\gamma_i^2)$, $i = 1,2$, and $E(\gamma_1\gamma_2)$, where E is again the expectation operator. The correlation coefficient ρ_Γ for γ_1 and γ_2 is

$$\rho_\Gamma = E(\gamma_1\gamma_2)/\sigma_{\gamma 1}\sigma_{\gamma 2} \quad , \tag{26a}$$

and a similar definition holds for ρ_χ associated with $\chi(D_s)$ and $\chi(v_s)$. Using Eqs. (24a) and (24c) as valid linear approximations for $\chi(D_s)$ and $\chi(v_s)$ in terms of γ_1 and γ_2, along with a modified version of Eq. (23b), the following formula for ρ_χ is derived:

$$\rho_\chi = (1 + \kappa\rho_\Gamma)/(1 + \kappa^2 + 2\kappa\rho_\Gamma)^{1/2} , \tag{26b}$$

where

$$\kappa \equiv \sigma_{\gamma_1}/\sigma_{\gamma_2} . \tag{26c}$$

It is important to observe that ρ_χ from Eq. (26b) is influenced solely by the correlation coefficient ρ_Γ, and the ratio κ of standard deviations associated with relative period and frequency perturbations. That is, it is independent of all mean-state quantities and constants in Eqs. (24a) and (24c).

We display in Fig. 8 graphs of ρ_χ versus ρ_Γ for various values of κ ranging from zero to infinity. From the $\kappa = 0$ and $\kappa = 0.5$ curves, associated with relatively small period-error standard deviations, ρ_χ is close to one. This indicates that relative errors in source depth and speed are nearly perfectly correlated (and nearly linearly related[22]), regardless of the correlation between period and frequency variations. As κ increases, the curves in Fig. 8 decrease monotonically. For large values of κ, ρ_χ approaches the diagonal $\kappa = \infty$. Thus, when the standard deviation of period perturbations is significantly greater than that associated with frequency, output-error correlation is virtually identical with the correlation between input variations. The fact that all curves in Fig. 8 begin at the points $(\rho_\Gamma,\rho_\chi) = (-1, \pm 1)$ and end at (1,1) shows that a perfect correlation between γ_1 and γ_2 always produces the same result in $\chi(D_s)$ and $\chi(v_s)$. The particular case $\kappa = 1$, with a discontinuity at $\rho_\Gamma = -1$, represents a transition between a situation where ρ_χ is never zero ($\kappa < 1$) and one where ρ_χ is always zero for some nonzero

value of ρ_χ ($\kappa > 1$). Finally, we conclude that if $\rho_\Gamma = 0$ (input perturbations are uncorrelated), then $\rho_\chi \neq 0$ (output errors possess some correlation), unless κ is large.

B. Tracker performance bounds

Next, we regard the received signal, from which phase-roll period and frequency measurements are obtained, as corrupted by noise. The noise N(t) is taken to be Gaussian with zero mean, spatially incoherent, and spectrally white with power N_0 in each one-Hertz band. We express the received signal Z(t) at R at time t as

$$Z(t) = W(t) + N(t) \ , \tag{27a}$$

where W is given by Eq. (4a). Errors in estimates for the period and received frequency are taken to possess Gaussian probability densities. As before, means of these descriptors, along with output source depth and speed values, are taken as known. With $t_1 = 0$ for convenience, the observation time T of measurements extends from - T/2 to T/2 s, and encompasses tens of seconds (see Sec. I). The time-averaged power S_0 of the signal is[23]

$$S_0 \equiv \lim_{T\to\infty} (1/T) \int_{-T/2}^{T/2} W^2(t)dt = (A_1^2 + A_2^2)/2 \ . \tag{27b}$$

One appropriate signal-to-noise ratio (SNR) here is then S_0/N_0. Cramer-Rao lower bounds[24] for the variances of unbiased estimators for the track outputs are desired, as functions of SNR. A two-stage estimation procedure[25] is required: First, obtain such bounds for variances of descriptors in terms of SNR; subsequently, express track output variance bounds in terms of those for descriptor variances.

For the first stage, the 2-vector $\underset{\sim}{\alpha}$ is defined with $\alpha_1 \equiv p_1$ and $\alpha_2 \equiv f_1$ as nondimensional versions of period and received frequency. Let $\Psi(\underset{\sim}{\alpha})$ denote

the symmetric 2 × 2 Fisher Information matrix[24] associated with $\underset{\sim}{\alpha}$. Applying the approach for sinusoidal signals in Ref. 4, it can be shown that $\Psi_{ij}(\underset{\sim}{\alpha})$, the ij^{th} entry of $\Psi(\underset{\sim}{\alpha})$, is given by

$$\Psi_{ij}(\underset{\sim}{\alpha}) = (1/N_0) \int_{-T/2}^{T/2} (\partial W/\partial \alpha_i)(\partial W/\partial \alpha_j) dt \ . \tag{28}$$

Entries of $\Psi(\underset{\sim}{\alpha})$ are evaluated from Eq. (28) by representing W as the sum of the two signals in Eq. (3a), expressing their phases $\phi_1(t)$ and $\phi_2(t)$ in terms of α_1 and α_2, and using the relatively large size of T to neglect small terms. Cramer-Rao lower bounds for the variances $\sigma^2(\hat{\alpha}_1)$ and $\sigma^2(\hat{\alpha}_2)$ of unbiased estimators of α_1 and α_2 are the diagonal elements $\Lambda_{11}(\underset{\sim}{\alpha})$ and $\Lambda_{22}(\underset{\sim}{\alpha})$ of the symmetric 2 × 2 matrix $\Lambda(\underset{\sim}{\alpha}) \equiv \left[\Psi(\underset{\sim}{\alpha})\right]^{-1}$. It follows that

$$\sigma^2(\hat{\alpha}_1) \geq \Lambda_{11}(\underset{\sim}{\alpha}) = (\overline{P}_1/2\pi)^2(12/T^3)(k + k^{-1})^2(S_0/N_0)^{-1} \tag{29a}$$

and

$$\sigma^2(\hat{\alpha}_2) \geq \Lambda_{22}(\underset{\sim}{\alpha}) = (1/2\pi\ \overline{f}_{r1})^2(12/T^3)(1 + k^2)(S_0/N_0)^{-1} \ , \tag{29b}$$

where k is given in Eq. (4d). We also require later the off-diagonal entry,

$$\Lambda_{12}(\underset{\sim}{\alpha}) = \Lambda_{21}(\underset{\sim}{\alpha}) = -(\overline{P}_1/2\pi\ \overline{f}_{r1})^2(12/T^3)(1 + k^{-2})(S_0/N_0)^{-1} \ . \tag{29c}$$

We note that Eqs. (29) depend on S_0/N_0, T, k, and the dimensional mean values of period and received frequency. It follows from Eqs. (28a) and (28b) that the Cramer-Rao lower bound associated with period perturbations α_1 is much greater than that for frequency perturbations α_2. Also, for our algorithm involving multipath information at a single receiver, bounds decrease as $1/T^3$ for increasing T. This qualitative result agrees with that reported[4] for differential Doppler estimation for single-path signals at multiple receivers.

Turning to the aforementioned second stage, we establish Cramer-Rao lower bounds associated with the 2-vector $\underset{\sim}{z}$, where $z_1 \equiv D_s/\overline{D}_r$ and $z_2 = x_{51}$ [from

Eq. (14c)] are nondimensional versions of source depth and speed. From the system of two equations for $p_1 = \alpha_1$ and $f_1 = \alpha_2$ described in Sec. III B, relations $\underset{\sim}{\alpha} = \underset{\sim}{\alpha}(\underset{\sim}{z})$ can be found. The ij^{th} entry Q_{ij} of the 2 × 2 Jacobian matrix Q for this new system is

$$Q_{ij} = \partial\alpha_i/\partial z_j \ , \tag{30}$$

where the partial derivatives are evaluated at mean values of $\underset{\sim}{z}$ components. For our situation,

$$Q_{11} = 2\bar{x}_{61}e_1|z_2 \cos \bar{\beta}_{s1} + \bar{v} \cos \bar{\beta}_{r1}|(1+e_1e_2)^{-3/2}[(1+\bar{z}_1)/(1-\bar{z}_1)^3] \ , \tag{31a}$$

$$Q_{12} = \bar{x}_6|\cos \bar{\beta}_{s1}|[(\cos \bar{\psi}_1/\cos \bar{\beta}_{r1}) - (1+e_1e_2)^{-1/2}] \ , \tag{31b}$$

$$Q_{22} = \bar{\varepsilon}\ x_6(\cos \bar{\beta}_{s1}/\cos \bar{\beta}_{r1})\cos \bar{\psi}_1 \ , \tag{31c}$$

where

$$e_1 \equiv (\cos \bar{\beta}_{r1}/\cos \bar{\psi}_1)^2 - 1, \ e_2 \equiv [(1+\bar{z}_1)/(1-\bar{z}_1)]^2 \ , \tag{31d}$$

and $\bar{\varepsilon}$, $\bar{v}$, and $\bar{x}_{61}$ are defined in Eqs. (14b) and (14c). Under our model assumptions, it follows[5] that the Fisher Information matrix $\Psi(\underset{\sim}{z})$ associated with $\underset{\sim}{z}$ is

$$\Psi(\underset{\sim}{z}) = \tilde{Q}\ \Psi(\underset{\sim}{\alpha})Q \ . \tag{32}$$

Cramer-Rao lower bounds associated with $\underset{\sim}{z}$ are the diagonal elements of $\Lambda(\underset{\sim}{z}) = [\Psi(\underset{\sim}{z})]^{-1}$, as before. From Eqs. (29), (31), and (32) and the definitions of z_1 and z_2, such bounds for the variances $\sigma^2(\hat{D}_s)$, $\sigma(\hat{v}_s)$ of unbiased estimators of D_s and v_s are

$$\sigma^2(\hat{D}_s) \geq \bar{D}_r^2\ Q_{11}^{-2}\ [\Lambda_{11}(\underset{\sim}{\alpha}) - 2(Q_{12}/Q_{22})\Lambda_{12}(\underset{\sim}{\alpha}) + (Q_{12}/Q_{22})^2\Lambda_{22}(\underset{\sim}{\alpha})] \tag{33a}$$

and

$$\sigma^2(\hat{v}_s) \geq (\bar{c}/\bar{P}_1 \bar{f}_{r1})^2 \, Q_{22}^{-2} \, \Lambda_{22}(\underset{\sim}{\alpha}) \, . \tag{33b}$$

From Eq. (33a) the lower bound on source depth variances depends on bounds for both period and received frequency variances. From Eq. (31b), the lower bound for speed variances depends only on the lower bound for received frequency variance. This result is analogous to one in Sec. III B for non-random error variations. We display in Fig. 9 graphs of the Cramer-Rao lower bounds for depth and speed error for special scenario (A) versus the dB SNR, $10 \log_{10} (S_0/N_0)$. The lower bounds are shown as percentage standard deviations, normalized via the mean value of each output. Measurement observation time used for both curves in Fig. 9 is T = 30 s. The very small values for the speed bound, of less than about 2%, corresponding to a speed error of less than 0.1 ms^{-1}, are noteworthy. They arise because of its aforementioned dependence on the received frequency lower bound. This bound, $\Lambda_{22}(\underset{\sim}{\alpha})$, is very small due to the quantity $(1/2\pi \, \bar{f}_{r1})^2$ in Eq. (29b). The depth bound in Fig. 9 decreases steadily from just under 30%, or 90 m, at a SNR of 0 to just under 10%, or 30 m, when the SNR is 10. This bound is influenced mainly by the phase-roll period variance bound, and is consequently larger than that for the speed curve. Results for scenarios (D) and (E) are very similar to those shown in Fig. 9. We conclude that variance bounds for the special scenarios are excellent for source speed and good for source depth at moderate to high SNR.

Our procedures could be extended to analyses of the more general scenarios. As illustrated in Sec. III, output errors tended to be comparable to or less than those associated with the scenarios considered here. Thus, it is anticipated that bounds on the performance of the full algorithm should be reasonable.

V. SUMMARY

This paper considers the passive determination of bearing, range, depth, course, speed, and frequency for a moving cw acoustic source S. Measurements are taken from a moving linear receiving array R. Both S and R are submerged at constant depths of less than 400 m, separated by ranges less than about 10 km, and they move on linear paths at constant speeds. The dominant acoustic signals are assumed to travel along two upper-ocean ray paths, one direct and one surface-reflected, and the sound speed is taken to be constant there. The tracking is accomplished using a new combination of acoustic quantities (or descriptors). These include the signal-arrival angle at R and the Doppler-shifted received frequency that are associated with the direct ray, as well as the phase-roll quasi-period of multipath phase variations. The latter involves regularly spaced, brief changes in total-field phase rate. Using descriptor measurements at two distinct times, a system of equations for the horizontal tracking algorithm is developed, relating descriptors to six unknown source parameters. Our algorithm formulation is sufficiently general so that it can be extended to more than two measurement times for additional improvement in source-parameter estimates. Solution examples via a least-squares numerical procedure are provided for various scenarios.

We then investigate the sensitivity of output values to variations in inputs, which include the descriptors and the sound speed. Such variations might result from measurement errors associated with noise, the receiving array, environmental fluctuations, and other factors. Procedures are presented for analyzing the effects of both deterministic and random input perturbations on output errors. The methods rely on efficiently obtaining linear approximations for output errors in terms of input variations. These

approximations are also computationally efficient, and results using them are shown to be valid for small, as well as somewhat larger, variations. Further, they are useful to express variances and covariances of localization errors in terms of those for random input variations.

We focus on three typical cases of perturbed inputs, associated with phase-roll periods and received frequencies, signal-arrival angles, and sound speed. Sensitivity of the tracking algorithm to these types of measurement errors is studied by considering a variety of S-R scenarios. In all configurations, small perturbations of all algorithm inputs produce small variations of output estimates. For example, in one scenario, percentage depth, range, and speed errors were less than 8% for relative errors in periods of up to 20%. However, some outputs are shown to be more sensitive to larger variations in certain inputs. Further insight into algorithm robustness is gained by considering special tracking scenarios, such as motion confined to a vertical plane, in which fewer than six source parameters are unknown. Our sensitivity analysis for these situations corroborates the algorithm robustness for input variations of reasonable magnitude.

For the special tracking cases, we develop tractable formulas for output errors for non-random and random input perturbations. These formulas are used to obtain both qualitative and quantitative information concerning relative effects of various descriptor errors. For the random variations, we analyze effects of phase-roll period and received-frequency perturbations on relative errors in source depth and speed. The influence of the correlation between perturbations in these descriptors, which are both related to travel-time variations due to S-R motion, on the correlation between relative output errors is determined. For example, if these inputs are perfectly correlated, then the same result for correlation holds for the outputs. If the standard deviation for phase-roll period variations is much greater than that for

frequency perturbations, the degree of correlation between output errors is nearly identical to the input-error correlation.

We also investigate the influence of a specific corrupting mechanism, namely Gaussian white noise, on the measurement of period and received frequency. Cramer-Rao lower bounds for variances of unbiased estimators for relative errors in source depth and speed, in terms of signal-to-noise ratio, are developed. These bounds on tracker performance are derived by using a two-stage estimation procedure applied to our algorithm. Examples for special S-R scenarios, which typically involve very small bounds on speed errors and percentage depth errors less than 15% for moderate to high signal-to-noise ratios, indicate good tracker performance.

[1] A. G. Lindgren and K. F. Gong, IEEE Trans. Aerosp. Electron. Syst. AES-14, 564-577 (1978).

[2] V. C. Aidala and S. C. Nardone, IEEE Trans. Aerosp. Electron. Syst. AES-18, 432-441 (1982).

[3] M. J. Hinich and M. C. Bloom, J. Acoust. Soc. Am. 69, 738-743 (1981).

[4] P. M. Schultheiss and E. Weinstein, J. Acoust. Soc. Am. 66, 1412-1419 (1979).

[5] P. M. Schultheiss and E. Weinstein, IEEE Trans. Acoust. Speech Signal Process. ASSP-29, 600-607 (1981).

[6] C. H. Knapp and G. C. Carter, J. Acoust. Soc. Am. 61, 1545-1549 (1977).

[7] G. C. Carter, IEEE Trans. Acoust. Speech Signal Process. ASSP-29, 463-470 (1981).

[8] J. C. Hassab, B. W. Guimond, and S. C. Nardone, J. Acoust. Soc. Am. 70, 1054-1061 (1981).

[9] R. E. Wilcox, J. Acoust. Soc. Am. 63, 870-875 (1978).

[10] K. F. Gong, "Multipath target motion analysis: properties and implications of the multipath process," Naval Underwater Syst. Center, New London, CT, NUSC Tech. Rep. 6657 (July 1982).

[11] J. L. Kays, M. J. Jacobson, and W. L. Siegmann, J. Acoust. Soc. Am. 69, 95-107 (1981).

[12] P. M. Schultheiss and E. Ashok, J. Acoust. Soc. Am. 74, 131-142 (1983).

[13] J. C. Hassab, J. Acoust. Soc. Am. 75, 479-485 (1984).

[14] D. J. Ramsdale and R. A. Howerton, J. Acoust. Soc. Am. 68, 901-906 (1980).

[15] M. J. Hinich and W. Rule, J. Acoust. Soc. Am. 58, 1023-1029 (1975).

[16] K. F. Gong, "Three-dimensional TMA in the presence of environmental influences," Naval Underwater Syst. Center, New London, CT, NUSC Tech. Rep. 6347 (December 1980).

[17] E. R. Robinson and A. H. Quazi, J. Acoust. Soc. Am. 77, 1086-1090 (1985).

[18] B. D. Steinberg and A. K. Luthra, J. Acoust. Soc. Am. 71, 630-634 (1982).

[19] R. N. Baer, J. Acoust. Soc. Am. 69, 70-75 (1981).

[20] J. Stoer and R. Bulirsch, Introduction to Numerical Analysis, translated from German by R. Bartels, W. Gautschi, and C. Witzgall, (Springer-Verlag, New York, 1980), Chap. 5.

[21] C. C. Lin and L. A. Segel, Mathematics Applied to Deterministic Problems in the Natural Sciences (MacMillan, New York, 1974), pp. 190-191.

[22] J. L. Melsa and A. P. Sage, An Introduction to Probability and Stochastic Processes (Prentice-Hall, Englewood Cliffs, NJ, 1973), Chap. 4.

[23] I. N. El-Behery and R. H. MacPhie, J. Acoust. Soc. Am. 62, 125-134 (1977).

[24] A. D. Whalen, Detection of Signals in Noise (Academic Press, New York, 1971), Chap. 10.

TABLE I. Values for parameters, descriptors, and outputs for scenarios (A)-(E) (c = 1520 ms-1, Δt_2 = 120 s).

Parameter, descriptor, or output.	Scenario (A)	(B)	(C)	(D)	(E)
D_r(m)	200	200	150	200	200
v_r(ms^{-1})	5	5	10	10	10
ψ_1(deg)	45.0	100.0	45.2	1.4	2.9
ψ_2	31.4	124.2	106.1	2.6	4.1
P_1(s/cycle)	22.0	6.2	12.4	27.4	21.3
P_2	9.0	11.4	22.1	8.5	10.9
f_{r1}(Hz)	503.49	994.40	503.74	504.93	501.64
f_{r2}	503.11	991.82	499.06	504.93	501.64
D_s(m)	300	300	300	300	300
R_1(m)	3000	2000	2000	4000	2000
R_2	1779	3316	1311	2200	1400
v_s(ms^{-1})	10	10	5	5	5
β_{r1}(deg)	45.0	100.0	-45.0	0	0
β_{r2}	31.2	124.3	-106.2	0	0
β_{s1}(deg)	-45.0	140.0	-30.0	0	180.0
β_{s2}	-58.8	164.3	-91.2	0	180.0
f_s(Hz)	500	1000	500	500	500

FIGURE LEGENDS

Fig. 1. (a) Vertical projection at time t_1 of S and R motions and ray arrivals. (b) Horizontal projection of S and R tracks between times t_1 and t_2. (c) Angles associated with direct ray at R.

Fig. 2. Top view (time t_1) of tracking scenarios (A)-(E).

Fig. 3. Percentage depth, range, and speed errors versus phase-roll period perturbation (s/cycle) at time t_2, (a) scenario (A), (b) scenario (B). Received frequency perturbation = 0.1 Hz.

Fig. 4. For scenario (C) at time t_2, percentage depth, range, and speed errors versus (a) phase-roll period perturbation (s/cycle) (received frequency perturbation 0.1 Hz), (b) received angle perturbation (deg).

Fig. 5. Bearing and course angle errors (deg) at time t_2 versus received angle perturbation (deg), (a) scenario (B), (b) scenario (C).

Fig. 6. Percentage depth, range, and speed errors at times t_1 and t_2 versus phase-roll period perturbation (s/cycle), (a) restricted scenario (A), (b) scenario (D). Received frequency perturbation 0.1 Hz.

Fig. 7. Percentage depth, range, and speed errors at times t_1 and t_2 versus received frequency perturbation (Hz), (a) restricted scenario (A), (b) scenario (E). Phase-roll period perturbation 1 s/cycle.

Fig. 8. Correlation coefficient of relative depth/speed errors versus correlation coefficient of period/received frequency perturbations, for several standard-deviation ratios κ in restricted scenarios.

Fig. 9. Cramer-Rao lower bounds for percentage normalized standard deviation of depth and speed versus signal-to-noise ratio (dB).

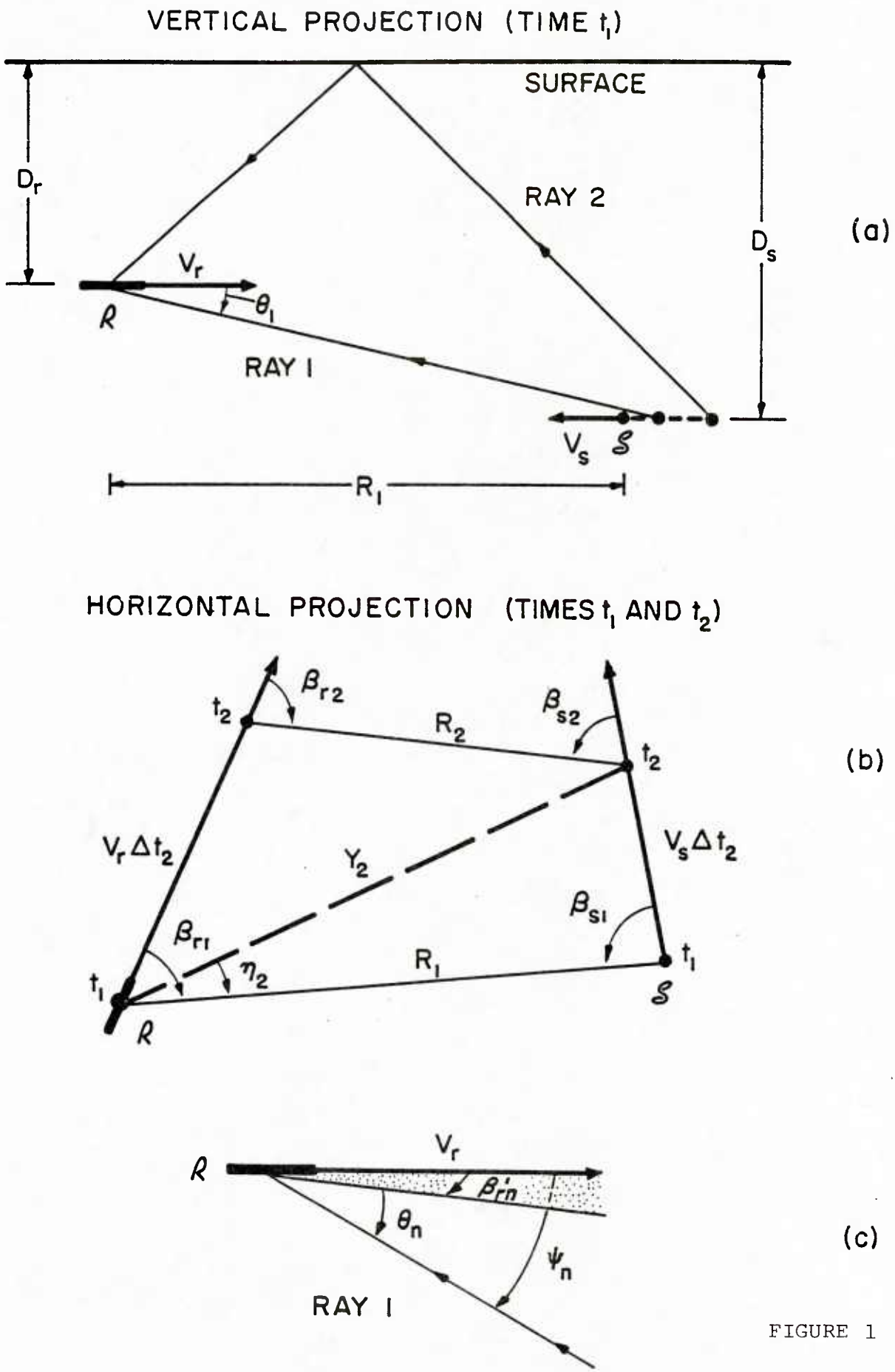
VERTICAL PROJECTION (TIME t_1)
SURFACE
D_r
RAY 2
D_s
(a)
V_r
θ_1
R
RAY 1
V_s
S
R_1
HORIZONTAL PROJECTION (TIMES t_1 AND t_2)
β_{r2}
t_2
R_2
β_{s2}
t_2
(b)
$V_r \Delta t_2$
Y_2
$V_s \Delta t_2$
β_{s1}
β_{r1}
η_2
R_1
t_1
t_1
S
R
V_r
R
β'_{rn}
θ_n
(c)
ψ_n
RAY 1

FIGURE 1

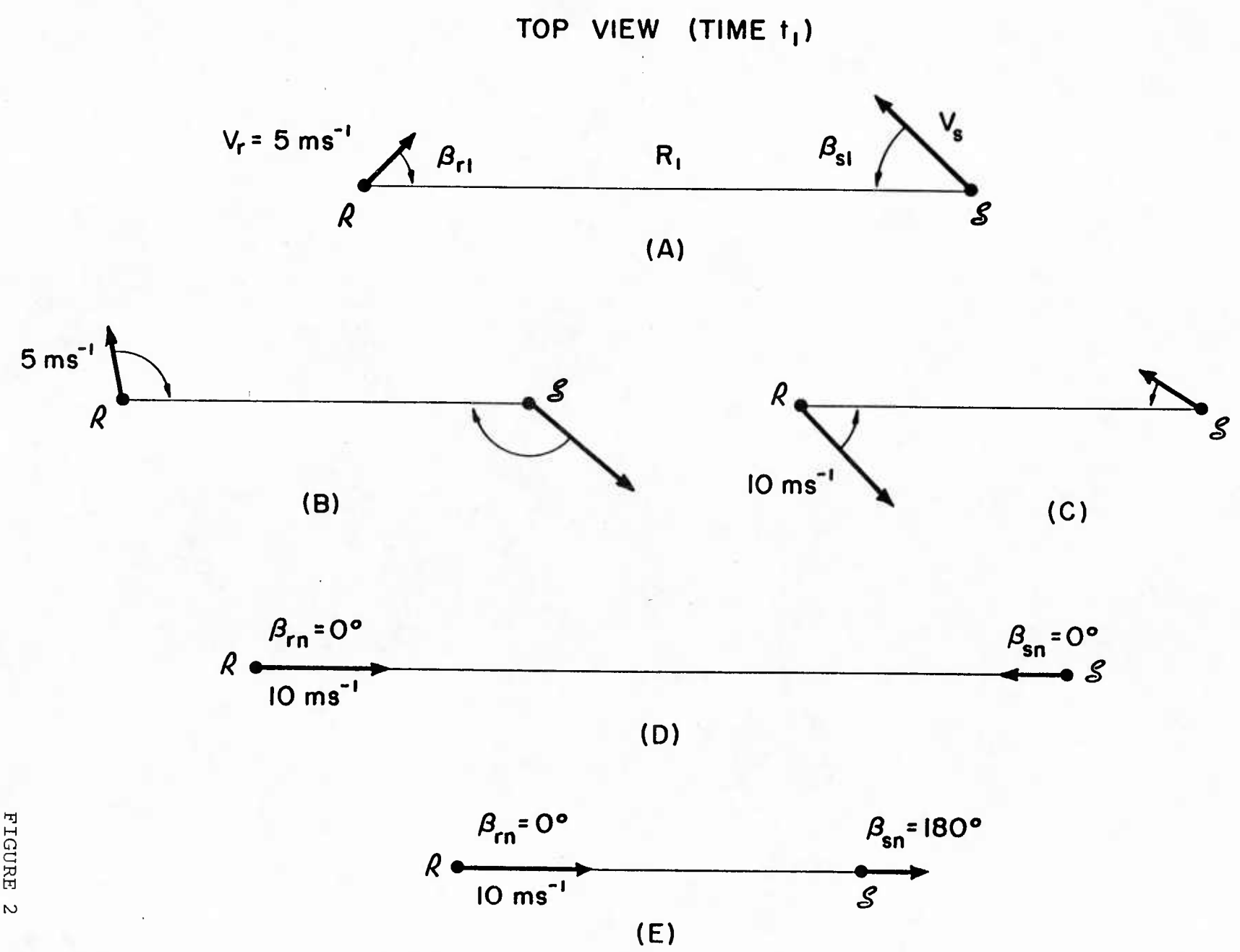
TOP VIEW (TIME t_1)
V_r = 5 ms^{-1}
β_{r1}
R_1
β_{s1}
V_s
R
S
(A)
5 ms^{-1}
R
S
(B)
R
S
10 ms^{-1}
(C)
β_{rn} = 0°
R
10 ms^{-1}
β_{sn} = 0°
S
(D)
β_{rn} = 0°
R
10 ms^{-1}
β_{sn} = 180°
S
(E)

FIGURE 2

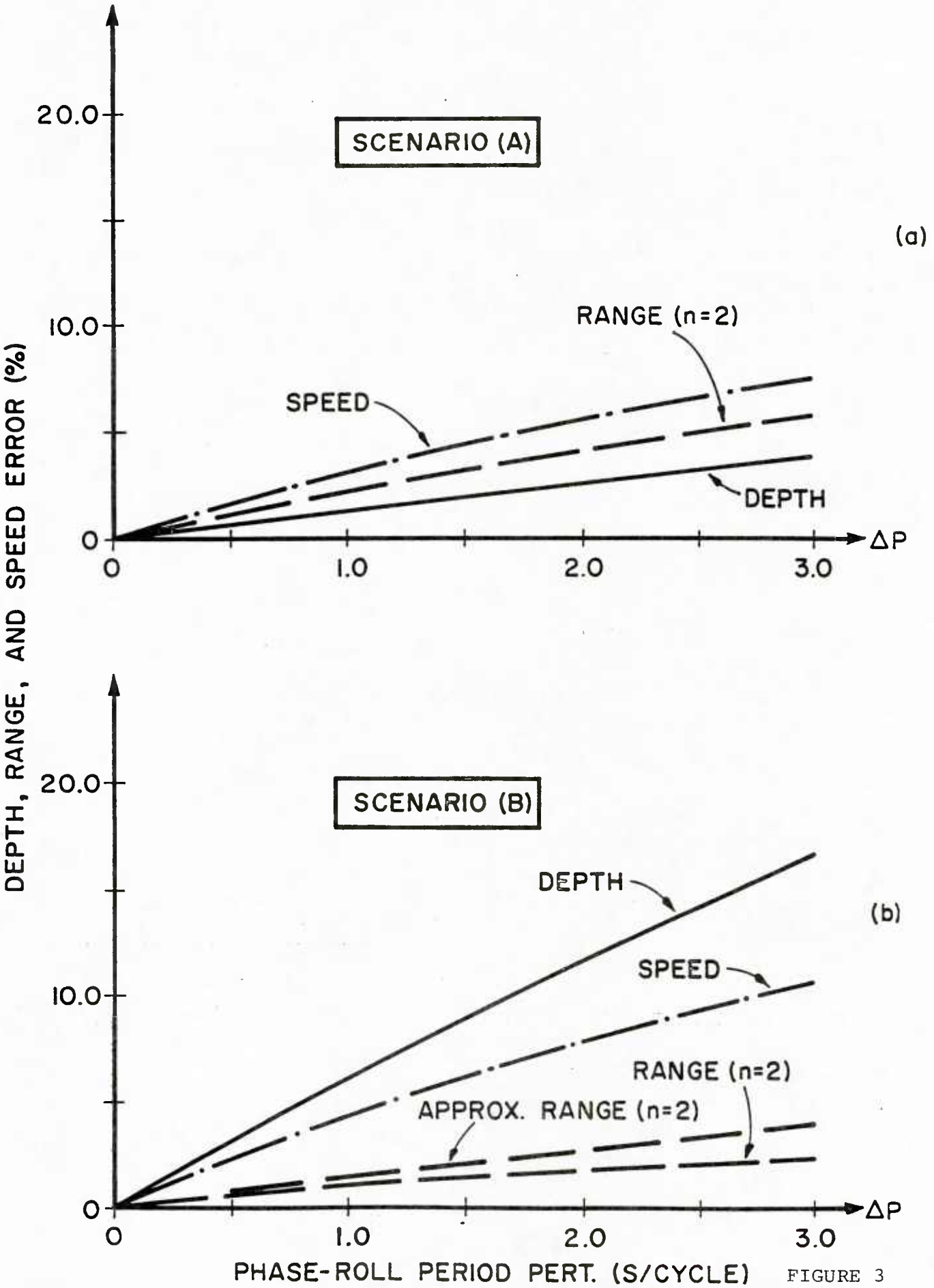
SCENARIO (A)
(a)
20.0
10.0
0
RANGE (n=2)
SPEED
DEPTH
ΔP
0
1.0
2.0
3.0
DEPTH, RANGE, AND SPEED ERROR (%)
SCENARIO (B)
(b)
DEPTH
SPEED
RANGE (n=2)
APPROX. RANGE (n=2)
PHASE-ROLL PERIOD PERT. (S/CYCLE)

FIGURE 3

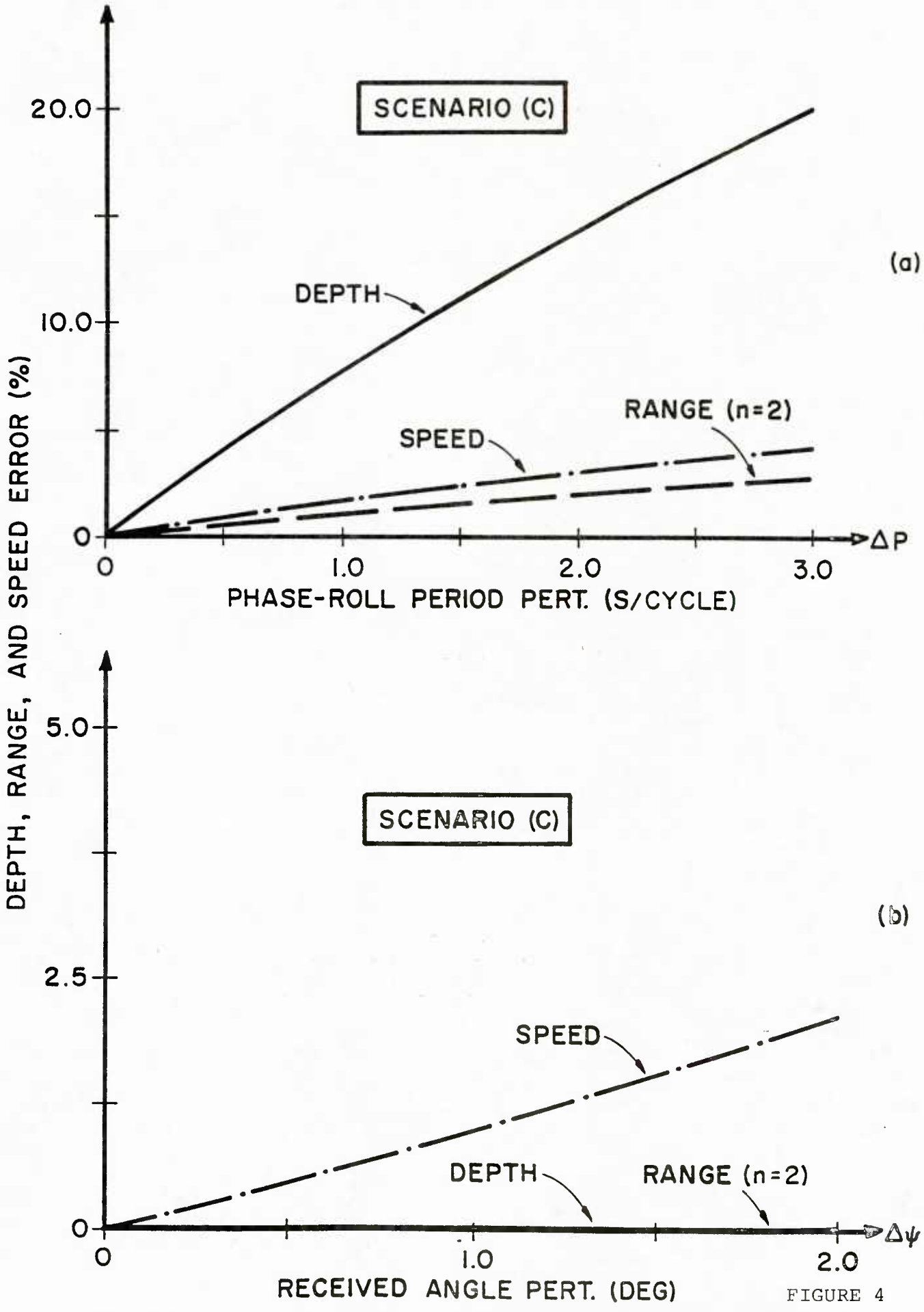
SCENARIO (C)
20.0
10.0
0
DEPTH
SPEED
RANGE (n=2)
ΔP
0
1.0
2.0
3.0
PHASE-ROLL PERIOD PERT. (S/CYCLE)
(a)
DEPTH, RANGE, AND SPEED ERROR (%)
SCENARIO (C)
5.0
2.5
0
SPEED
DEPTH
RANGE (n=2)
Δψ
0
1.0
2.0
RECEIVED ANGLE PERT. (DEG)
(b)

FIGURE 4

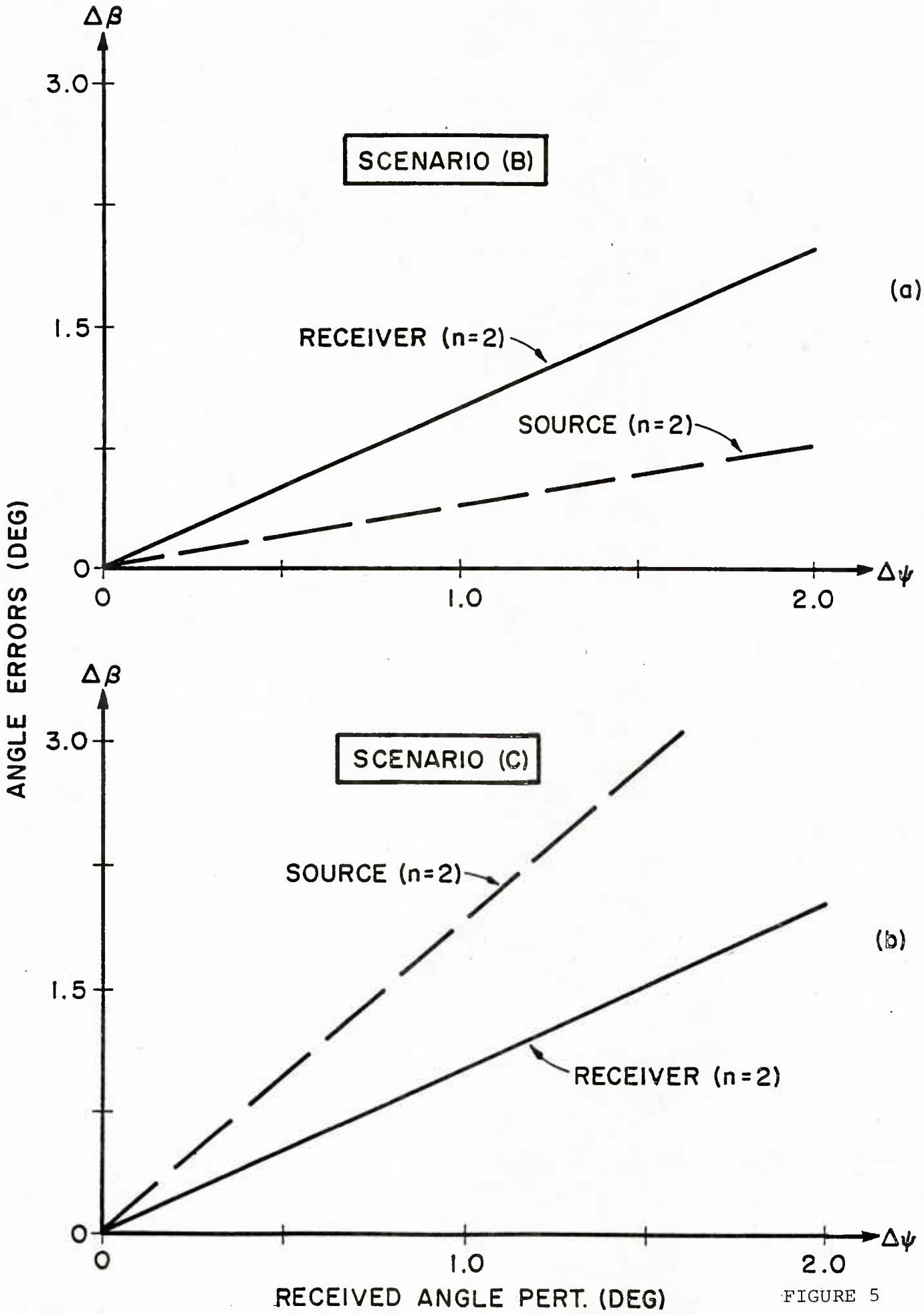
Δβ
3.0
1.5
0
SCENARIO (B)
RECEIVER (n=2)
SOURCE (n=2)
(a)
Δψ
0
1.0
2.0
ANGLE ERRORS (DEG)
Δβ
3.0
SCENARIO (C)
SOURCE (n=2)
(b)
1.5
RECEIVER (n=2)
0
Δψ
0
1.0
2.0
RECEIVED ANGLE PERT. (DEG)

FIGURE 5

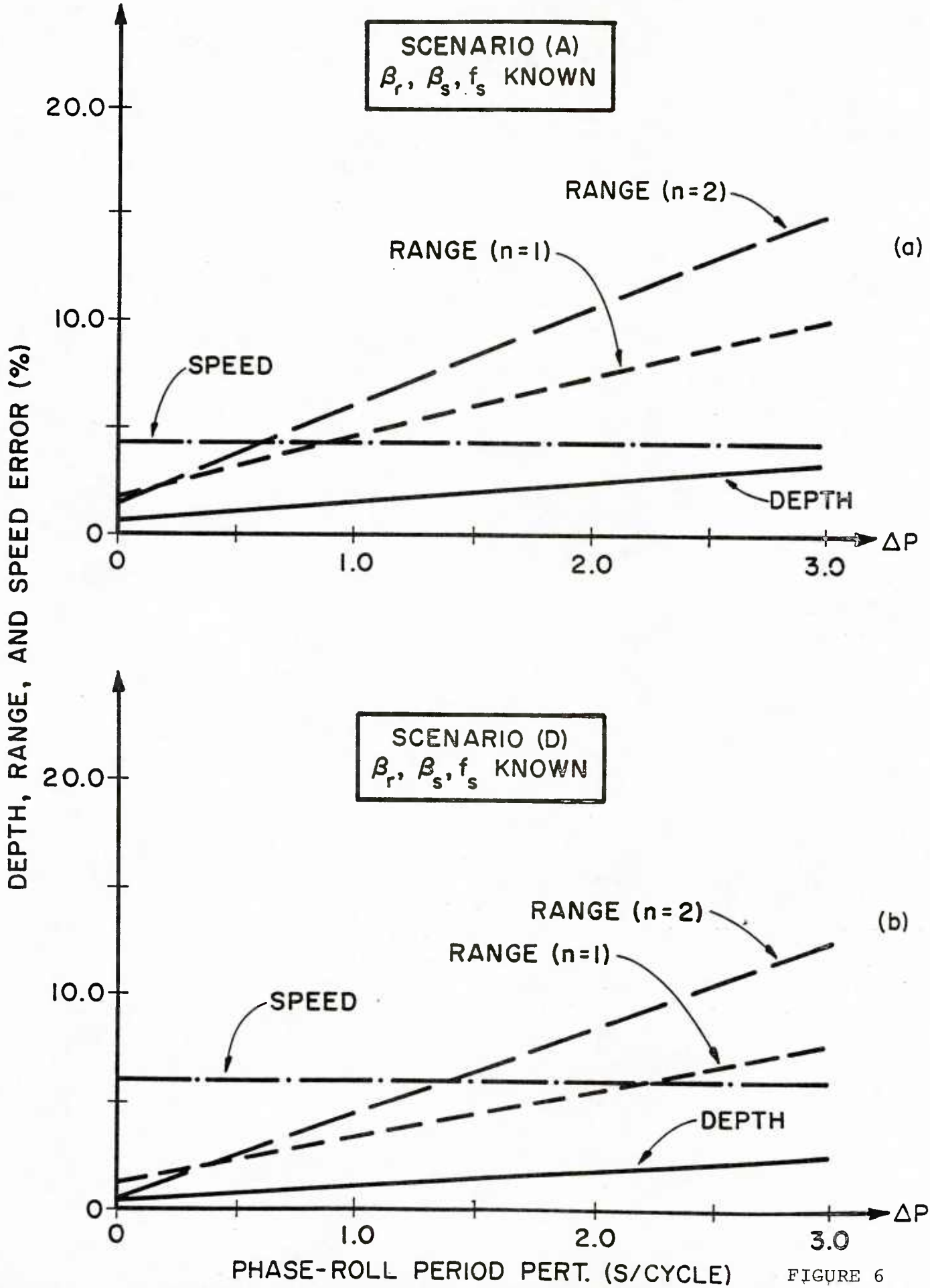
SCENARIO (A)
β_r, β_s, f_s KNOWN
20.0
10.0
0
RANGE (n=2)
RANGE (n=1)
(a)
SPEED
DEPTH
0
1.0
2.0
3.0
ΔP
SCENARIO (D)
β_r, β_s, f_s KNOWN
20.0
10.0
0
RANGE (n=2)
RANGE (n=1)
(b)
SPEED
DEPTH
0
1.0
2.0
3.0
ΔP
DEPTH, RANGE, AND SPEED ERROR (%)
PHASE-ROLL PERIOD PERT. (S/CYCLE)

FIGURE 6

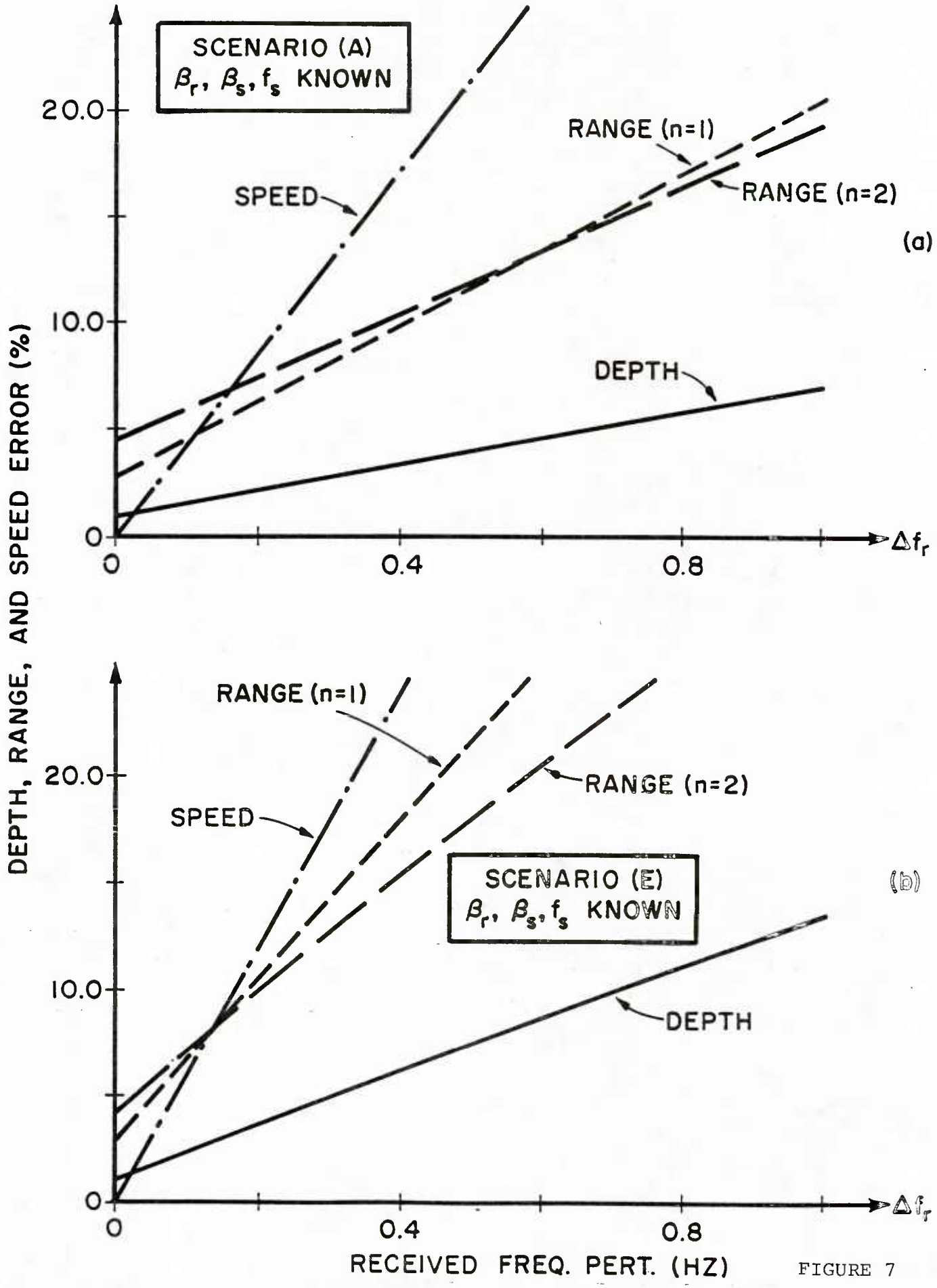
SCENARIO (A)
β_r, β_s, f_s KNOWN
RANGE (n=1)
RANGE (n=2)
SPEED
DEPTH
(a)
20.0
10.0
0
0
0.4
0.8
Δf_r
SCENARIO (E)
β_r, β_s, f_s KNOWN
RANGE (n=1)
RANGE (n=2)
SPEED
DEPTH
(b)
20.0
10.0
0
0
0.4
0.8
Δf_r
DEPTH, RANGE, AND SPEED ERROR (%)
RECEIVED FREQ. PERT. (HZ)

FIGURE 7

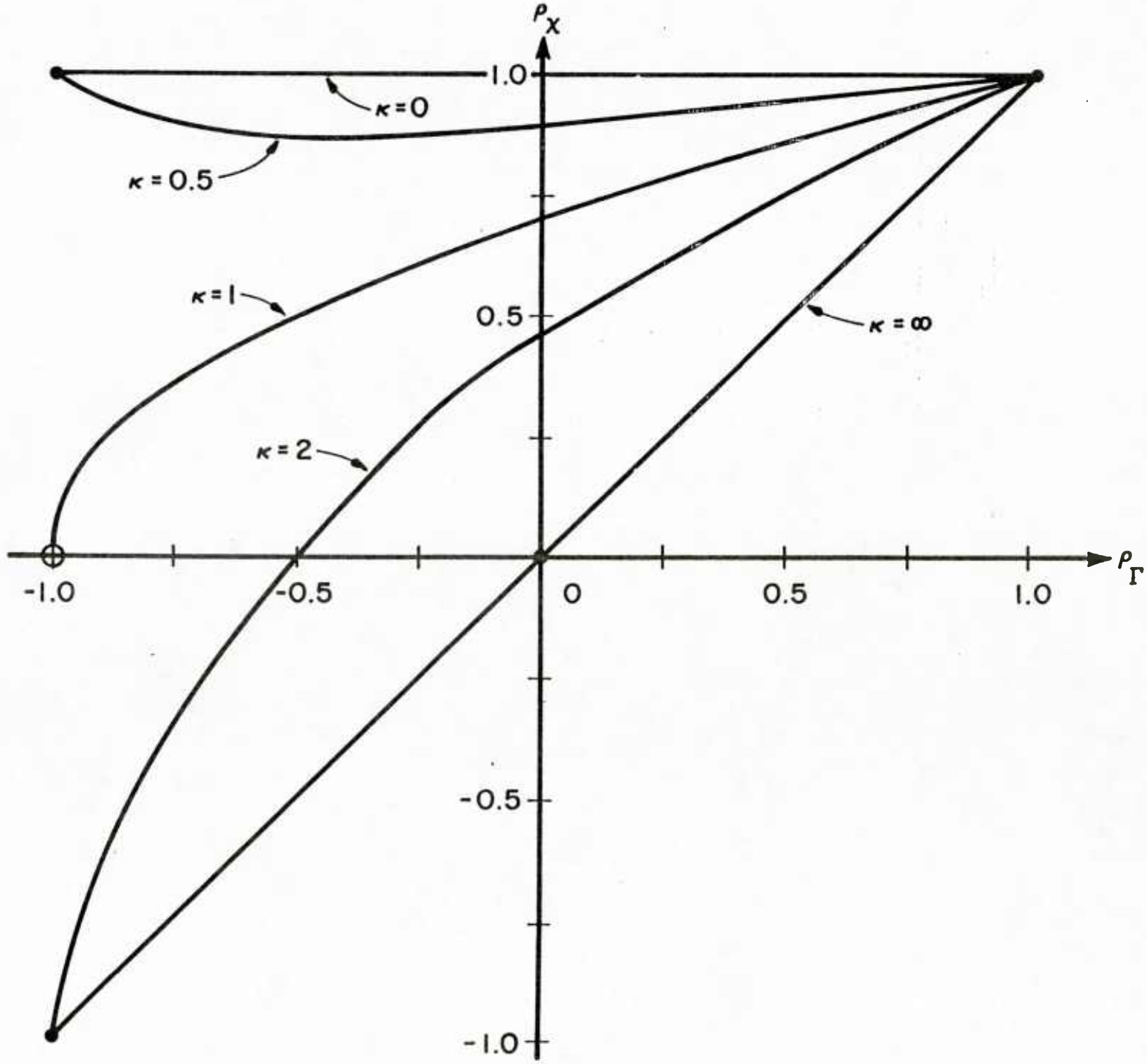
ρ_X
1.0
$\kappa = 0$
$\kappa = 0.5$
$\kappa = 1$
0.5
$\kappa = \infty$
$\kappa = 2$
ρ_Γ
-1.0
-0.5
0
0.5
1.0
-0.5
-1.0
CORRELATION COEFF., DEPTH/SPEED ERRORS
CORRELATION COEFF., PERIOD/FREQ. ERRORS

FIGURE 8

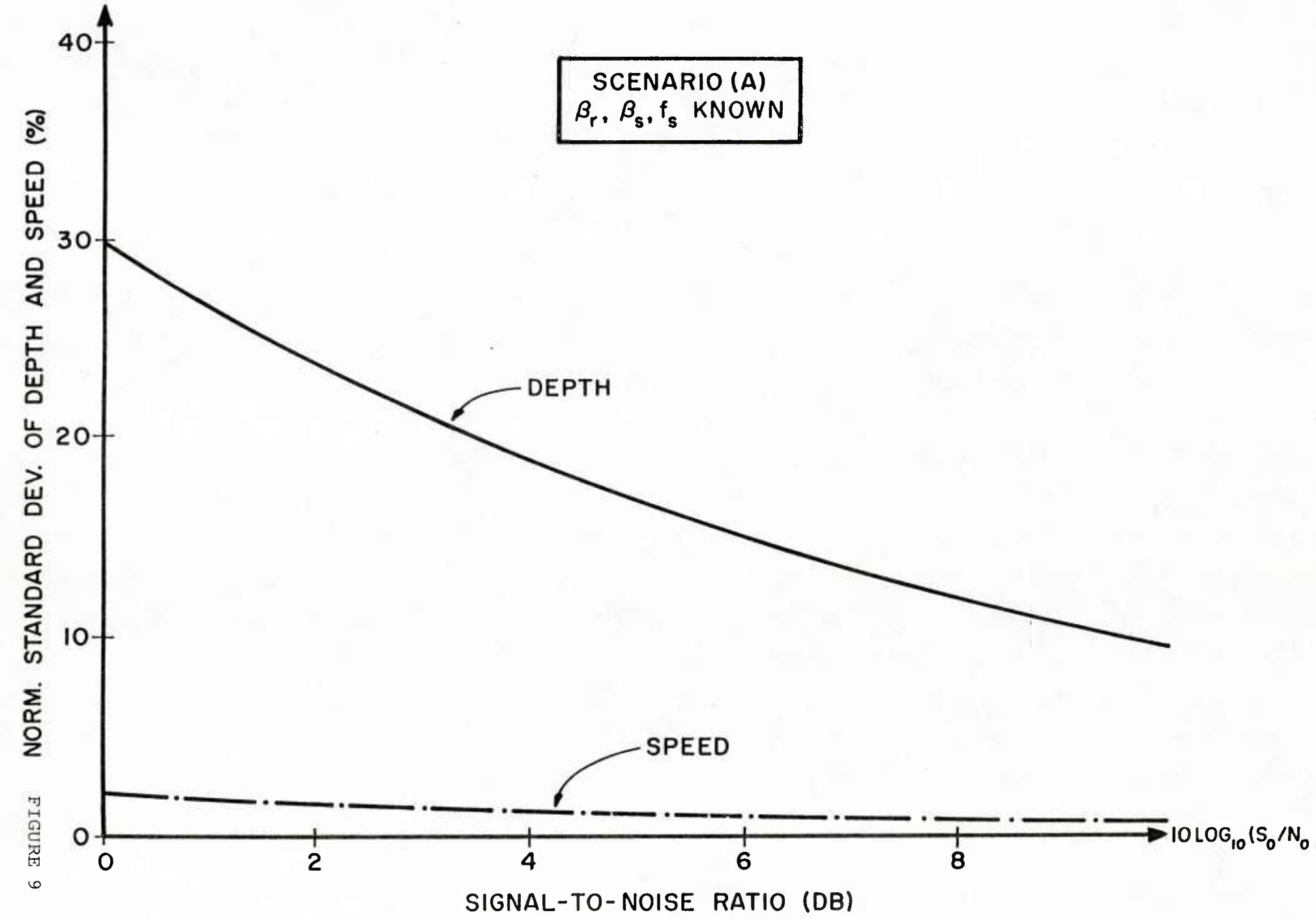
SCENARIO (A)
β_r, β_s, f_s KNOWN
NORM. STANDARD DEV. OF DEPTH AND SPEED (%)
40
30
20
10
0
DEPTH
SPEED
0
2
4
6
8
$10 \log_{10}(S_0/N_0)$
SIGNAL-TO-NOISE RATIO (DB)

FIGURE 9

UNCLASSIFIED
DISTRIBUTION LIST
DEC 1981

Addressee	No. of Copies
Office of Naval Research 800 North Quincy Street Arlington, Virginia 22217	
Attn: Code 425AC	2
102	1
102C	1
210	1
220	1
Office of Naval Technology 800 North Quincy Street Arlington, Virginia 22217	
Attn: MAT 0721	1
MAT 0724	1
Director Naval Research Laboratory 4555 Overlook Avenue, SW. Washington, D.C. 20375	
Attn: Dr. J. C. Munson	1
Mr. R. R. Rojas	1
Dr. B. B. Adams	1
Dr. W. B. Moseley	1
Dr. J. P. Dugan	1
Unclassified Library	1
Superintendent Naval Research Laboratory Underwater Sound Reference Division P.O. Box 8337 Orlando, Florida 32806	1
Director Office of Naval Research Branch Office 1030 East Green Street Pasadena, California 91106	1
Office of Naval Research Rm 239, Campbell Hall University of California Berkeley, California 94720	1
Director Office of Naval Research Branch Office 495 Summer Street Boston, Massachusetts 02210	1
Office of Naval Research New York Area Office 715 Broadway - 5th Floor New York, New York 10003	1
Commanding Officer Office of Naval Research Branch Office Box 39 FPO New York 09510	1
Director Office of Naval Research Branch Office 536 South Clark Street Chicago, Illinois 60605	1
Office of Naval Research Resident Representative University District Building, Room 422 1107 North East 45th Street Seattle, Washington 98105	1

Addressee	No. of Copi
Technical Director Naval Oceanographic Research and Development Activity NSTL Station Bay St. Louis, Mississippi 39522	
Attn: Technical Director	1
Dr. L. Solomon	1
Dr. R. Gardner	1
Mr. E. Chaika	1
Mr. R. Van Wyckhouse	1
Dr. S. W. Marshall	1
Director Naval Oceanographic Office NSTL Station Bay St. Louis, Mississippi 39522	
Attn: Mr. H. Beck	1
Dr. T. M. Davis	1
Mr. W. H. Geddes	1
Dr. W. Jobst	1
Mr. R. Merrifield	1
Mr. R. A. Peloquin	1
Dr. M. K. Shank	1
Office of the Assistant Secretary of the Navy for Research, Engineering and Systems Washington, D.C. 20350	
Attn: Dr. D. Barbe, Rm 4E732 Pentagon	1
Dr. J. H. Probus, Rm 5E779 Pentagon	1
Chief of Naval Operations Room 5D580, Pentagon Washington, D.C. 20350	
Attn: OP951F	1
Commander Naval Sea Systems Command Department of Navy Washington, D.C. 20362	
Attn: Capt. James M. Van Metre PMS 409	1
Chief of Naval Operations Office of the Director Naval Oceanographic Division OP-952 Department of the Navy Washington, D.C. 20352	
Attn: Dr. R. W. James	1
Capt. J. C. Harlett	1
Commander Oceanographic System, Atlantic Box 100 Norfolk, Virginia 23511	1
Commander Oceanographic System, Pacific Box 1390 Pearl Harbor, Hawaii 96860	1

Addressee	No. of Copies
Defense Advanced Research Projects Agency 1400 Wilson Boulevard Arlington, Virginia 22209 Attn: Capt. V. Simmons	1
ARPA Research Center Moffett Field Unit #1 California 94035 Attn: Mr. E. Smith	1
Commanding Officer Fleet Weather Central Box 113 Pearl Harbor, Hawaii 96860	1
Naval Ocean Systems Center (Kaneohe) Kaneohe, Hawaii 96863 Attn: Mr. D. Hightower Mr. B. Kishimoto Mr. R. Buecher	1 1 1
Commander Naval Electronic Systems Command 2511 Jefferson Davis Highway National Center #1 Arlington, Virginia 20360 Attn: CAPT C. A. Rose,, PME 124 LCDR P. Girard, NAVELEX 612	2
Commander Naval Air Systems Command Jefferson Plaza #1 1411 Jefferson Davis Highway Arlington, Virginia 20360	1
Commander Naval Sea Systems Command National Center #2 2521 Jefferson Davis Highway Arlington, Virginia 20362 Attn: SEA 63R 63Y	1 1
Commanding Officer Fleet Numerical Weather Central Monterey, California 93940 Attn: Mr. Paul Stevens Dr. D.R. McLain (NMFS)	1 1
Defense Documentation Center Cameron Station Alexandria, Virginia 22314	12
Commander Naval Ocean Systems Center Department of the Navy San Diego, California 92132 Attn: Dr. Daniel Andrews Dr. Dean Hanna Mr. Henry Aurand Dr. Harry A. Schenck	1 1 1 1

Addressee	No. of Copies
Commander Naval Surface Weapons Center Acoustics Division Silver Spring, Maryland 20910	1
Commander Naval Surface Weapons Center Science and Mathematics Research Group (K05) Dahlgren, Virginia 22448 Attn: Dr. E.W. Schwiderski	1
Commanding Officer Naval Underwater Systems Center New London Laboratory New London, Connecticut 06320 Attn: Dr. William Von Winkle Dr. A. Nuttall Mr. A. Ellinthorpe Dr. D.M. Viccione Mr. A. Donn Cobb	1 1 1 1 1
Commander Naval Air Development Center Department of the Navy Warminster, Pennsylvania 18974 Attn: Unclassified Library	1
Commanding Officer Naval Coastal Systems Laboratory Panama City, Florida 32401 Attn: Unclassified Library	1
Commanding Officer Naval Underwater Systems Center Newport Laboratory Newport, Rhode Island 02840 Attn: Unclassified Library	1
Commander David W. Taylor Naval Ship Research and Development Center Bethesda, Maryland 20084 Attn: Dr. M. Sevik	1
Superintendent Naval Postgraduate School Monterey, California 93940	1
Superintendent U.S. Naval Academy Annapolis, Maryland 21402 Attn: Library	1
Commanding Officer Naval Intelligence Support Center 4301 Suitland Road Washington, D.C. 20390 Attn: NISC 20	1
Director Applied Physics Laboratory University of Washington 1013 North East 40th Street Seattle, Washington 98105 Attn: Dr. T.E. Ewart Dr. M. Schulkin	1 1

Addressee	No. of Copies
Applied Research Laboratories University of Texas at Austin P.O. Box 8029 10000 FM Road 1325 Austin, Texas 78712	
Attn: Dr. Loyd Hampton	1
Dr. Charles Wood	1
Atlantic Oceanographic and Meteorological Laboratories 15 Rickenbacker Causeway Miami, Florida 33149	
Attn: Dr. John Proni	1
Bell Telephone Laboratories 1 Whippany Road Whippany, New Jersey 07981	
Attn: Dr. Bruce Bogart	1
Dr. Peter Hirsch	1
Bolt, Beranek, and Newman, Inc. 50 Moulton Street Cambridge, Massachusetts 02238	
Attn: Dr. K. L. Chandiramani	1
Chase, Inc. 14 Pinckney Street Boston, Massachusetts 02114	
Attn: Dr. David Chase	1
Dr. David Middleton 127 East 91st Street New York, New York 10028	1
Duke University Department of Electrical Engineering Durham, North Carolina 27706	
Attn: Dr. Loren Nolte	1
General Electric Company Heavy Military Electronic Systems Syracuse, New York 13201	
Attn: Mr. Don Winfield	1
General Electric Company P.O. Box 1088 Schenectady, New York 12301	
Attn: Dr. Thomas G. Kincaid	1
Gould, Incorporated Chesapeake Instrument Division 6711 Baymeadow Drive Glen Burnie, Maryland 21061	
Attn: Dr. O. Lindemann	1
G R Associates, Inc. 10750 Columbia Pike Suite 602 Silver Spring, Maryland 20901	
Attn: Dr. Sheldon Gardner	
Dr. Frank Rees	
Hughes Aircraft Company P.O. Box 3310 Fullerton, California 92634	
Attn: Mr. S. W. Autrey	1

Addressee	No. of Copies
Hydroacoustics, Inc. 321 Northland Ave. P.O. Box 3818 Rochester, New York 14610	1
Institute for Acoustical Research Miami Division for the Palisades Geophysical Institute 615 South West 2nd Avenue Miami, Florida 33130	
Attn: Mr. M. Kronengold	1
Dr. J. Clark	1
Institute of Geophysics and Planetary Physics Scripps Institute of Oceanography University of California La Jolla, California 92093	
Attn: Dr. W. Munk	1
Mr. J. Spiesberger	1
Jaycor Incorporated 205 South Whiting Street Suite 607 Alexandria, Virginia 22304	
Attn: Dr. S. Adams	1
Massachusetts Institute of Technology Acoustics and Vibration Laboratory 70 Massachusetts Avenue Room 5-222 Cambridge, Massachusetts 02139	
Attn: Professor Patrick Leehey	1
Palisades Sofar Station Bermuda Division of Palisades Geophysical Institute FPO New York 09560	
Attn: Mr. Carl Hartdegen	1
Polar Research Laboratory 123 Santa Barbara Avenue Santa Barbara, California 93101	
Attn: Mr. Beaumont Buck	1
Research Triangle Institute Research Triangle Park Durham, North Carolina 27709	
Attn: Dr. S. Huffman	1
Rensselaer Polytechnic Institute Troy, New York 12181	
Attn: Dr. Melvin J. Jacobson	
Science Applications, Inc. 8400 Westpark Drive McLean, Virginia 22102	
Attn: Dr. P. Tatro	
S.D.P. Inc. 15250 Ventura Boulevard Suite 518 Sherman Oaks, California 91403	
Attn: Dr. M. A. Basin	1

Addressee	No. of Copies
Texas Instruments, Inc. 13500 North Central Expressway Dallas, Texas 75231 Attn: Mr. Charles Black	1
Underwater Systems, Inc. 8121 Georgia Avenue Silver Spring, Maryland 20910 Attn: Dr. M. Weinstein	1
University of Miami Rosenstiel School of Marine and Atmospheric Sciences 4600 Rickenbacker Causeway Miami, Florida 33149 Attn: Dr. H. DeFerrari	1
University of Michigan Department of Aerospace Engineering, North Campus Ann Arbor, Michigan 48109 Attn: Dr. W. W. Wilmarth	
University of Michigan Cooley Electronics Laboratory Ann Arbor, Michigan 48105 Attn: Dr. T. G. Birdsall	
University of Rhode Island Department of Electrical Engineering Wakefield, Rhode Island 02881 Attn: Dr. Donald Tufts	1
Woods Hole Oceanographic Institution Woods Hole, Massachusetts 02543 Attn: Dr. Paul McElroy Dr. R. Spindel	1 1